APS physics

CHORUS

This is the accepted manuscript made available via CHORUS. The article has been published as:

Laser melting modes in metal powder bed fusion additive manufacturing

Cang Zhao, Bo Shi, Shuailei Chen, Dong Du, Tao Sun, Brian J. Simonds, Kamel Fezzaa, and Anthony D. Rollett

Rev. Mod. Phys. **94**, 045002 — Published 20 October 2022

DOI: 10.1103/RevModPhys.94.045002

Laser melting modes in metal powder bed fusion additive manufacturing

Cang Zhao*, Bo Shi, Shuailei Chen, Dong Du
Department of Mechanical Engineering, Tsinghua University, Beijing 100084, China,
Key Laboratory for Advanced Materials Processing Technology, Ministry of Education, Beijing 100084, China,
and Beijing Key Lab of Precision/Ultra-precision Manufacturing Equipments and Control, Tsinghua University,
Beijing 100084, China.

Tao Sun
Department of Materials Science and Engineering, University of Virginia, Charlottesville, VA 22904, USA.

Brian J. Simonds
Applied Physics Division, Physical Measurements Laboratory, National Institute of Standards and Technology,
Boulder, CO 80305, USA.

Kamel Fezzaa
X-ray Science Division, Argonne National Laboratory, Lemont, IL 60439, USA.

Anthony D. Rollett
Department of Materials Science and Engineering, Carnegie Mellon University, Pittsburgh, PA 15213, USA,
and NextManufacturing Center, Carnegie Mellon University, Pittsburgh, PA 15213, USA.

*cangzhao@tsinghua.edu.cn

In laser powder bed fusion additive manufacturing of metals, extreme thermal conditions create many highly dynamic physical phenomena such as vaporization and recoil, Marangoni convection, and protrusion and keyhole instability. Collectively however, the full set of phenomena is too complicated for practical applications and, in reality, the melting modes are used as a guideline for printing. With increasing local material temperature beyond the boiling point, the mode can change from conduction to keyhole. These mode designations ignore laser-matter interaction details but in many cases are adequate to determine the approximate microstructures and hence the properties of the build. To date, no consistent, common, and coherent definitions have been agreed upon because of historic limitations in melt pool and vapor depression morphology measurements. Here, we distinguish process-based definitions of different melting modes from those based on postmortem evidence. The latter are mainly derived from the transverse cross-sections of the fusion zone, whereas the former come directly from time-resolved x-ray imaging of melt pool and vapor depression morphologies. These process-based definitions are more strict and physically sound, and they offer new guidelines for laser additive manufacturing practices and create new research directions. We highlight the significance of the keyhole, which substantially enhances the laser energy absorption by the melt pool. Recent studies strongly suggest that stable-keyhole laser melting enables efficient, sustainable, and robust additive manufacturing. The realization of this scenario demands the development of multiphysics models, signal translations from morphology to other feasible signals, and in-process metrology across platforms and scales.

CONTENTS

I. INTRODUCTION

Metal additive manufacturing (AM, commonly referred to as 3D printing) is an industrial application of rapid prototyping (RP) of metal parts (Kruth *et al.*, 1998; Campbell *et al.*, 2012). It was originally derived from the alliance of welding methods and powder-based technologies. The direct powder deposition into a laser melted pool gave rise to direct laser fabrication (DLF) and laser engineered net shaping (LENS) technologies (Lewis *et al.*, 1994; Griffith *et al.*, 1996; Atwood *et al.*, 1998; Lewis and Schlienger, 2000) that, while effective, lacked the resolution to be generally useful without post machining and were not helped by low deposition rate. Once, however, the original patents had expired, the development of powder bed systems quickly revealed that good resolutions and reasonable build rates enabled direct manufacturing of complex geometries and (almost) fully dense parts. It was this development that took 3D printing from the status of rapid prototyping to actual (additive) manufacturing of end-use products.

Metal AM, by definition, is a collection of disruptive technologies that fabricate metal parts directly from digital computer-aided design and drafting (CADD) models, usually layer upon layer (ISO/ASTM 52900-15, 2015). In comparison to conventional subtractive or formative manufacturing, this emerging cluster offers unprecedented design freedom and manufacturing capabilities for multiscale, multi-material, and multifunctional optimization and integration (Frazier, 2014; Herzog *et al.*, 2016; MacDonald and Wicker, 2016; Onuike *et al.*, 2018; Leach *et al.*, 2019; Gu *et al.*, 2021; Sing *et al.*, 2021). Also, metal AM requires a short supply chain, which becomes increasingly critical when considering global supply chain disruption risks (Thomas, 2016; Kurpjuweit *et al.*, 2021). The on-site and on-demand manufacturing capability can largely reinforce economic and societal resiliency and sustainability. As a result, metal AM has been evolving rapidly during the past decade and is transforming the aeronautic, aerospace, automotive, defense, chemical, medical, and energy industries (Martin *et al.*, 2017; Gisario *et al.*, 2019; Joint Defense Manufacturing Council, 2021). Here are a few examples. Topologically optimized components (e.g., graded lattice structures) can be built via metal AM to largely reduce the buy-to-fly ratio (weight ratio of raw material and final part) of an aircraft (Gaynor and Guest, 2016; Maconachie *et al.*, 2019). Sensors and actuators can be seamlessly embedded into a component for structural health monitoring and assessment (Hossain *et al.*, 2016; Juhasz *et al.*, 2020). Metal implants customized to each patient can be quickly built using AM, and it is now possible to tailor the elastic modulus and stiffness to mimic human bone (Sing *et al.*, 2016; Wang *et al.*, 2016).

Of all the competing metal AM technologies, laser powder bed fusion (LPBF, aka selective laser melting) is currently the most commonly used (Thijs *et al.*, 2010; Frazier, 2014; Khairallah *et al.*, 2016; Zhao *et al.*, 2020). In a LPBF process, a laser beam of high power density is scanned across a thin layer of metal powder (e.g., less than 100 μm thickness) to locally and selectively melt the powder and fuse it to a previous layer. Typically, spherical powder particles are favored because of their high flowability which improves powder bed uniformity and part quality (Heiden *et al.*, 2019; Brika *et al.*, 2020). Benefiting from the small sizes of laser beam (e.g., ~100 μm) and powder particles (typically, 10 μm - 60 μm), and correspondingly small melt pool width (e.g., ~200 μm in the transverse direction), LPBF enables high dimensional accuracy and extreme flexibility in fabricating complex features and structures (Wu *et al.*, 2020; Seltzman and Wukitch, 2021). The high cooling rates (e.g., 10^6 K/s) associated with the small melt pool and fast laser scanning promote high solidification rates, which refines the grains and opens up new avenues and opportunities for developing innovative materials with far-from-equilibrium phases and improved properties, for example, new alloys that work under extremely harsh environments (e.g., outer space, deep oceans, and nuclear plants) where extreme temperatures, pressures, shocks, radiations, or corrosions exist (Kyo *et al.*, 1995; Hou *et al.*, 2020; Mohr *et al.*, 2020; McEnerney *et al.*, 2021). Furthermore, the digital nature of LPBF allows flexible control of processing conditions during the build of a single part. When using the same laser parameters, the uniform processing condition throughout the part eliminates much of the variability with casting such as macro-segregation, for example (Wang *et al.*, 2017; Agrawal *et al.*, 2020). When implementing various parameters, the material microstructures can be adjusted at various locations of the part, offering enhanced performance induced by the heterogeneity (Sun *et al.*, 2019; Sofinowski *et al.*, 2021).

LPBF is effectively an extension of laser welding at a small scale, which means, however, that it is subject to many of the same limitations. For example, LPBF parts are vulnerable to hot cracking due to dendritic growth during solidification and substantial residual stress (Martin *et al.*, 2017; Zhang *et al.*, 2017). This has largely limited the range of compositions to which LPBF can be applied, i.e., predominantly only weldable alloys. Meanwhile, many aspects of the LPBF-produced microstructures differ strongly from those conventionally produced, with features such as cellular structures, high dislocation content, super-saturation,

nano-precipitation, non-equilibrium phases, inclusions, and irregular grain structures (Herzog *et al.*, 2016; Martin *et al.*, 2017; Wang *et al.*, 2018; Voisin *et al.*, 2021). Some of these unique structures are beneficial, while others can deteriorate performance. For some alloys, the overall densities of LPBF parts are generally excellent (e.g., 99.5% of the theoretical density), but the complex laser and powder conditions can generate anomalies and occasionally structural defects, e.g., variable melt pools, porosity, and cracks (Wu *et al.*, 2014; Chiang *et al.*, 2019; Scime and Beuth, 2019a; Dowling *et al.*, 2020; Zhao *et al.*, 2020; Mostafaei *et al.*, 2022; Zhao *et al.*, 2022). This is one of the main factors currently hindering a wider application of LPBF in some industries. To manufacture defect-free and microstructure-controllable parts, we need a more comprehensive understanding of the interaction between laser and matter and the mode of laser melting.

In LPBF of metals, the mode of melting is one of the most fundamental concepts (Paul and Debroy, 1988; Fabbro and Chouf, 2000; King *et al.*, 2015; Cunningham *et al.*, 2019; Chen *et al.*, 2020; Zhao *et al.*, 2020). Generally, it consists of conduction and keyhole modes (Semak and Matsunawa, 1997; Rai *et al.*, 2007; King *et al.*, 2014; Aboulkhair *et al.*, 2016; Scipioni Bertoli *et al.*, 2017b; Forien *et al.*, 2020; Jadhav *et al.*, 2021). Between these two modes, it is also often believed that there exists a transition mode (Lee *et al.*, 2002; Verhaeghe *et al.*, 2009; Qi *et al.*, 2017; Simonds *et al.*, 2018; Ye *et al.*, 2019; Liu *et al.*, 2020; Tenbrock *et al.*, 2020; Gan *et al.*, 2021). These modes, regardless of the absence of detailed and complicated laser-matter interactions, largely determine the microstructures and defects as well as the performances of the product (Sames *et al.*, 2016; Cunningham *et al.*, 2017a; Wei *et al.*, 2017; Zhao *et al.*, 2017; Liu and Shin, 2019; Sun *et al.*, 2019; Hu *et al.*, 2020; Polonsky *et al.*, 2020; Roehling *et al.*, 2020; Martin *et al.*, 2021). For example, melting in keyhole mode can potentially refine grain structure, improve material strength, and mitigate cracking; when unstable, however, it can lead to keyhole porosity and degrade corrosion resistance and fatigue life (Aboulkhair *et al.*, 2014; Cunningham *et al.*, 2017a; Roehling *et al.*, 2020; Huang *et al.*, 2022).

Despite their crucial role in the research and development mentioned above, these melting modes have not yet achieved consistent, common, and coherent definitions. This shapes the motivation for this short review. Traditionally and experimentally, the postmortem transverse cross-section (perpendicular to the laser path) of a fused melt pool is used to distinguish the modes (Paul and Debroy, 1988; Assuncao *et al.*, 2012; King *et al.*, 2014; Qi *et al.*, 2017; Scipioni Bertoli *et al.*, 2017b; Simonds *et al.*, 2018; Ye *et al.*, 2019). Such a postmortem-based approach is simple and common in the community. However, the information of the vapor depression is missing and the boundaries of the modes are subjective and confusing (King *et al.*, 2014; Simonds *et al.*, 2018). Recently, the *operando* high-speed synchrotron x-ray imaging technique has enabled the community to refine and revise those long-standing definitions because of its micrometer spatial resolution, sub-nanosecond temporal resolution, MHz frame rate, and millimeter penetration capacity (Zhao *et al.*, 2017; Calta *et al.*, 2018; Leung *et al.*, 2018; Miyagi *et al.*, 2018; Parab *et al.*, 2018; Martin *et al.*, 2019b; Zhao *et al.*, 2019; Hocine *et al.*, 2020). The revised definitions come directly from the time-resolved measurements of the melt pool and vapor depression morphology evolutions (Cunningham *et al.*, 2019; Chen *et al.*, 2020; Zhao *et al.*, 2020). Compared to the postmortem-based version, these process-based definitions are clearer and more strict in physics. But so far, they have not yet attracted sufficient attention.

In this review, we employ the following terminologies when referring to the vapor-dominated cavity inside the melt pool. In general, the term "vapor depression" applies to any shape of cavity caused by the recoil momentum from vaporization of the liquid surface. It is more general and inclusive. The term "keyhole" is a subtype of the "vapor depression". It comes from the welding community in the early days of deep penetration technologies (electron-beam and laser-beam) (Miller and Takenaka, 1964; Elmer *et al.*, 2011), but has evolved into a broader concept (Cunningham *et al.*, 2019). Traditionally, the keyhole refers to a deep and narrow vapor cavity that is derived mainly from the postmortem transverse cross-section of a deep and narrow fused melt pool (Kaplan, 1994; Fabbro and Chouf, 2000; Cho and Na, 2006; Tan *et al.*, 2013; King *et al.*, 2014; Ye *et al.*, 2019). It is somewhat of an approximation that is confined to the keyhole melting mode. Here, the term "keyhole" is reserved for those depressions that are prone to multiple reflection and thus increased absorption. It can be, but not limited to, a deep and narrow morphology.

This short review is presented as follows. First, we describe the general physical process of laser heating. After briefly summarizing the complexity, we review two key coupled phenomena: melting and evaporation, and protrusion and keyhole instability. These physical phenomena drive the morphological evolution of the melt pool (with or without a vapor cavity) and are the foundation of melting mode definitions. Then, we assign the definitions to two categories on the basis of the morphology measurement approach. One is based on postmortem examination and the other on *in situ* visualizations. We emphasize and encourage the latter and discuss it in the order of *conceptual definitions*, *strict definitions*, and *from stationary to scanning*. In the end, we discuss the perspectives for practical implementations of the definitions and conclude the review.

II. GENERAL PHYSICAL PROCESS OF LASER MELTING

A. Complexity

The laser melting of a metal is a highly dynamic and complicated physical process (Markl and Körner, 2016; Guo *et al.*, 2018; Kouraytem *et al.*, 2019; Zhao *et al.*, 2019; Panwisawas *et al.*, 2020; Wang *et al.*, 2020; Zhao *et al.*, 2020). As illustrated in Fig. 1, it potentially involves all four fundamental states of matter – solid, liquid, vapor, and plasma. It also includes not only melting but also vaporization and recoil, Marangoni convection, vapor impact, multiple reflection and absorption, melt pool oscillations, protrusion and keyhole instability, and so forth.

It is the extreme thermal conditions caused by rapid heating that create these highly dynamic physical phenomena. Usually, the heating and cooling rates are on the order of 10^3 K/s to 10^8 K/s (Farshidianfar *et al.*, 2016; Yang *et al.*, 2016; Scipioni Bertoli *et al.*, 2017a; Zhao *et al.*, 2017; Hooper, 2018; Heigel *et al.*, 2020; Thampy *et al.*, 2020), the peak thermal gradient inside the melt pool is on the order of 10^6 K/m to 10^8 K/m (Gäumann *et al.*, 1999; Griffith *et al.*, 1999; Bontha *et al.*, 2006; Thijs *et al.*, 2013; Hooper, 2018; Roehling *et al.*, 2020; Zhao *et al.*, 2020), and the average temperature on the vapor depression walls can be hundreds of Kelvin above the boiling point of the metal (Zhao *et al.*, 2019; Pordzik and Woizeschke, 2020; Zhao *et al.*, 2020).

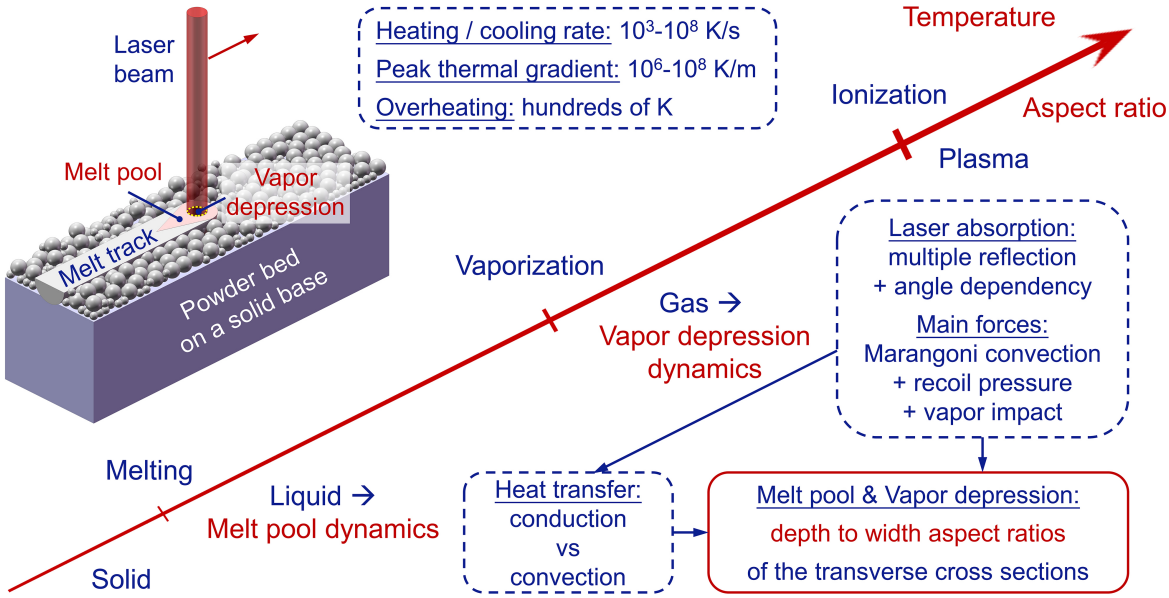

FIG. 1. The general physical process of laser melting. With the rapid increase in temperature, the solid (a powder bed sample here) transforms into liquid, gas, and plasma through the transitions of melting, vaporization, and ionization. During this process, melt pool and vapor depression form and evolve, and their depth-to-width aspect ratios of the transverse cross-sections continue to rise because of enhanced laser absorption and limited heat transfer. In the schematic on the top left corner, the approximate location of the vapor depression inside the melt pool is outlined with a yellow dashed circle, and the red arrow indicates the laser scan direction.

B. Melting and vaporization

1. At the atomic scale

The interaction between a high-power, continuous-wave or short-duration (longer than a nanosecond) pulsed laser and a metal can be considered in terms of a balance between photon absorption and phonon emission. The process is referred to as photothermal because the absorbed energy is directly transferred into heat on that timescale (i.e., dwell time or pulse width is longer than electron-phonon or even phonon-phonon relaxation time) (Link *et al.*, 1999; El-Sayed, 2001; Brown and Arnold, 2010; Dowden, 2017). For metals, it is often the metallic bonds that join atoms through the electrostatic attraction between valence electrons and ionized cores. During the laser AM process, the rapid local heating by the high-power laser excites atomic vibrations and deforms and breaks the bonds to melt and vaporize the metal. Unlike the slow and uniform heating that occurs in an oven, metallic bond deformation and breaking under high-power laser illumination initially only occurs within a thin surface layer because of limited optical absorption depth (e.g., ~10 nm) and thermal diffusion length (e.g., a few μm in 1 μs) (Wellershoff *et al.*, 1999; Lide, 2004; Foroozmehr *et al.*, 2016; Zhao *et al.*, 2019). The required thermal energy mainly depends on the number and strength of the bonds because of their generally isotropic nature (Campbell, 2008; Daeneke *et al.*, 2018). The bond number is associated with the material mass of surface layer and the atomic configuration like crystal structure of solid phase. The bond strength is generally related to the delocalization degree of valence electrons.

As the energy absorption increases, mostly due to single-photon interactions (Brown and Arnold, 2010), the intense collisions by free electrons enable some ionized cores to move away permanently from their equilibrium positions. The atomic motion becomes chaotic and the non-linear multi-phonon interactions trigger phase transformations (i.e., melting or change of crystalline phase). For example, in a pure solid metal with a coordination number of 10 (averaged over FCC and BCC crystals), melting starts when about 10 percent of the total metallic bonds inside the confined regime are loosened (but not yet broken). When the melting is complete, the crystal structure is completely lost and the shear modulus becomes zero, although short-range order may be preserved (Gur and Pan, 2008; Kenel *et al.*, 2017; Zhao *et al.*, 2017). In contrast, vaporization takes place only when a surface bond is broken (i.e., the kinetic energy obtained by an atom is in excess of the bond energy, on the order of a few eV) and the atoms in the vapor phase then move independently.

Under equilibrium conditions, the enthalpies required to change the phases from solid to liquid and from liquid to vapor are the latent heats of fusion and vaporization, respectively. The corresponding melting and boiling temperatures or the entropies of fusion and vaporization at a given pressure are constant. However, because of the rapid heating by the high-power laser, the actual phase transition temperatures or entropy values deviate from those characteristic points or equilibrium limits (Miotello and Kelly, 1999; Lorazo *et al.*, 2003; Kruth *et al.*, 2004; Ramirez-San-Juan *et al.*, 2010; Zhao *et al.*, 2019). For example, the liquid metal directly beneath the laser beam is often in a superheated state and additional energy is required to break the bonds and release the atoms. This situation is further complicated for multiphase alloys, in which the melting and vaporization could be highly heterogeneous as a result of the distinct strengths of the bonds between various alloy elements.

2. At the micro scale

Under stationary laser beam illumination, the metal, either plate or powder bed, is locally heated. When the temperature reaches the melting point, the metal forms a melt pool. The melt pool is initially small and shallow (Fig. 5(a)), and the heat is transported to the surrounding metal through thermal conduction (Eagar and Tsai, 1983; Assuncao *et al.*, 2012; Panwisawas *et al.*, 2017; Zhao *et al.*, 2017). Over time, the volume of the pool increases, as does the surface temperature, because laser heating at this stage outpaces thermal diffusion (Lee *et al.*, 2002; Rai *et al.*, 2007; Gusarov and Smurov, 2010). When the temperature is above the boiling point, local boiling occurs. On the free side of the surface layer, the metal vapor is ejected mainly along the local normal direction and towards the free space. On the other side, a recoil momentum pushes the liquid below the sample surface, in a direction opposite to vapor ejection (Semak and Matsunawa, 1997; Fabbro *et al.*, 2006; Verhaeghe *et al.*, 2009; Ly *et al.*, 2017; Bidare *et al.*, 2018; Zhao *et al.*, 2019). The flux of the vapor and the pressure of the recoil depend on the local overheating relative to the boiling point (Anisimov and Khokhlov, 1995; Semak and Matsunawa, 1997; Zhao *et al.*, 2019). Typically, for a stationary laser beam with a Gaussian profile, the surface region directly beneath the beam center achieves the highest temperature and overheating (Doubenskaia *et al.*, 2013; Yadroitsev *et al.*, 2014). As a result, the vapor is largely ejected upwards and the liquid is pushed downwards, creating a cavity called a vapor depression (Zhao *et al.*, 2017; Cunningham *et al.*, 2019). Generally, the melt pool and the vapor depression are nearly semicircular and symmetric. The entrance of powder particles into the laser beam or directly into the melt pool, however, could momentarily break the symmetry and create complex three-dimensional topologies (Zhao *et al.*, 2017; Wolff *et al.*, 2019; Li *et al.*, 2020; Lin *et al.*, 2020). At high power, as laser heating continues, the cavity may become deep enough that the reflected light encounters another region of the cavity interior before eventually escaping, which is colloquially referred to as multiple reflection (Kaplan, 1994; Cho and Na, 2006; Tan *et al.*, 2013). Every time the light irradiates a melt surface, additional energy is absorbed, the fraction of which, for a given material, depends on its local angle of incidence. In the field of laser fusion AM, this phenomenon is often referred to as “Fresnel absorption”. Since this term implies assumptions of how the absorption is quantified (mathematically by Fresnel equations), we prefer just “absorption” or “angle-dependent absorption” when referring to the phenomenon in general. Because of the positive feedback between cavity depth and laser absorption, the cavity may eventually become a deep and narrow shape (Matsunawa *et al.*, 1998; Lee *et al.*, 2002; Panwisawas *et al.*, 2017; Zhao *et al.*, 2017; Cunningham *et al.*, 2019). This was recently confirmed through real-time and simultaneous laser absorption and cavity depth measurements (Allen *et al.*, 2020). As the cavity grows, the melt pool deviates from its initially semicircular morphology (in general) and may show either a deep and conical shape (Fig. 5(c)) or a bimodal shape with a bowl on the top and a spike at the bottom [Fig. 4(a2)] (King *et al.*, 2014; Zhao *et al.*, 2017; Simonds *et al.*, 2018; Cunningham *et al.*, 2019). Inside the melt pool, the large thermal gradients, mostly around the vapor depression walls, promote convective mass and heat transfer. The heat transfer, though limited, confines the growth of the melt pool (Lee *et al.*, 2002; Rai *et al.*, 2007; Gusarov and Smurov, 2010).

When the laser beam is scanned by galvo mirrors, the melt pool morphology in the transverse cross-section remains nearly symmetric. However, in the longitudinal cross-section, the symmetry is broken as there always exists a tail at the end of the pool (Matsunawa *et al.*, 1998; Parab *et al.*, 2018). Ahead of the beam, solid metal is absorbed by an advancing melt, and behind it, the melt solidifies. Under steady-state laser scanning, on the sample surface, both the melting and solidification rates are equal to the scan velocity (Boettinger

et al., 1984; Kurz *et al.*, 1986). At low applied energy density (i.e., power divided by scan velocity), the melt pool is small, shallow, and more rounded (King *et al.*, 2014; Scipioni Bertoli *et al.*, 2017b). With increasing energy density, the pool becomes deeper and larger, and the surface starts to vaporize and deform, creating a vapor depression with asymmetric morphology on the longitudinal cross-section (Cunningham *et al.*, 2019). The front wall of the vapor depression is tilted, whose angle can be determined by the drill rate and scan velocity of the laser (Fabbro and Chouf, 2000; Cunningham *et al.*, 2019). Generally, the laser beam mostly impinges on this front wall, producing overheating and a strong vapor ejection along its normal and against the scan direction (Kaplan, 1994; Zhao *et al.*, 2019). However, at high applied energy density (e.g., high laser power and low scan velocity), a deep and narrow vapor cavity instigates downward multiple reflections of the light (Kaplan, 1994; Cho and Na, 2006; Tan *et al.*, 2013), leading to maximal temperatures at its bottom. This causes upward vapor ejection, which can resemble the stationary laser beam case (Bidare *et al.*, 2018; Cunningham *et al.*, 2019).

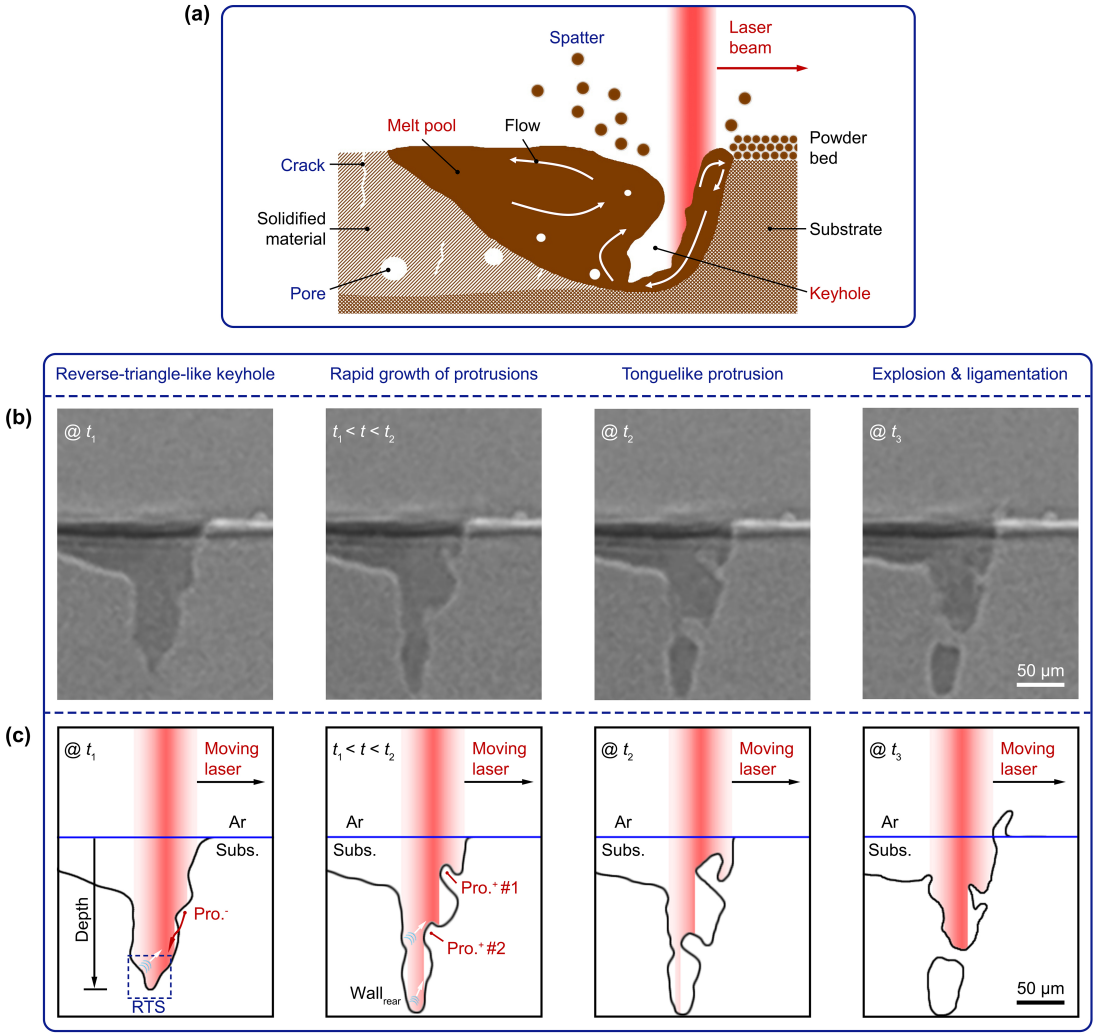

FIG. 2. Melt pool, keyhole, and common defects in unstable-keyhole-mode melting. (**a**) Schematic showing the general melt pool structure. The white arrows inside the melt pool indicate the flow pattern of the melt. (**b-c**) Protrusion structure on the front wall of an unstable keyhole. (**b**) High-speed high-energy x-ray images. (**c**) Schematic illustrations. At time t_1, a keyhole of reverse-triangle-like shape (RTS) forms. The rear wall is directly exposed to the incident laser beam, and the generated vapor then travels upwards towards the front wall, as indicated by the blue arc lines and white arrows in (**c**). Upon the collision with the vapor, the existing protrusions (e.g., Pro. #1 and Pro. #2) change from a dome shape leaning downward (denoted by Pro.$^-$) to a rod shape tilting upward (denoted by Pro.$^+$). Here, the rapid growth and collapse of a tongue-like protrusion Pro. #1 eventually leads to the formation of extremely fast ligaments and spatters, and the collapse of the protrusion Pro. #2 causes the formation of an instant keyhole pore. Panels (**b-c**) adapted from Zhao *et al.*, 2019.

C. Protrusion and keyhole instability

In both stationary and scanning cases, when the laser heating intensifies by, for example, increasing power or dwell time (interaction time or laser spot size divided by scan velocity) of the laser beam, the resulting deep keyhole can lead to instabilities. The consequences are mainly two-fold, as illustrated in Fig. 2(a). Above the sample surface, the vapor ejection shows chaotic behavior and some extremely fast spatters may be observed (Bidare *et al.*, 2018; Zhao *et al.*, 2019). Inside the sample, bubbles generated from the keyhole bottom tip can be accelerated by acoustic waves or viscous drag, and thus potentially captured by the advancing solidification front as pore defects (Zhao *et al.*, 2017; Bayat *et al.*, 2019; Kiss *et al.*, 2019; Zhao *et al.*, 2020; Zhao *et al.*, 2022). The keyhole pores are either vacuum or gas-filled after complete condensation depending on the processing environment and powder conditions (Weingarten *et al.*, 2015; Cunningham *et al.*, 2016; Kosonen *et al.*, 2021; Huang *et al.*, 2022). They differentiate from the gas entrainment pores that are caused by the environmental gas being trapped into the melt pool, which does not necessarily involve a highly unstable keyhole (Martin *et al.*, 2019a; Hojjatzadeh *et al.*, 2020).

The extremely fast spatters and keyhole pores are directly related to a structure on the front keyhole wall called protrusion (Zhao *et al.*, 2019; Zhao *et al.*, 2020). For example, in Figs. 2(b) and 2(c), under a scanning continuous-wave laser beam, the solid phase ahead of the front keyhole rim is heated, melted, and vaporized, forming a small vapor depression and a dome-shaped protrusion (Zhao *et al.*, 2019). This protrusion, propelled by the recoil momentum from the intense vaporization of its top surface layer (10^5 Pa to 10^6 Pa, orders of magnitude higher than the capillary and thermocapillary forces) (Kroos *et al.*, 1993; Lee *et al.*, 2002; Tan *et al.*, 2013; Kouraytem *et al.*, 2019), flows down along the front keyhole wall. Through statistical analysis of the protrusion speed, the average temperature on the front wall can be estimated to reach hundreds of Kelvin above the boiling point (Anisimov and Khokhlov, 1995; Semak and Matsunawa, 1997). Under certain laser irradiation conditions, the keyhole bottom becomes a reverse-triangle-like (or inverted-triangle-like) shape. A following protrusion, Pro. #1, appears at the front wall rim and flows downwards. During the down-flow process, the bottom surface of the protrusion is believed to be supported by the directional collision of the vapor that is strongly ejected from the bottom of the rear wall, causing a shape change from a dome leaning downward to a rod tilting upward. The protrusion then appears to stop running down and rest for a while. Meanwhile, with the scanning of the beam, new melt forms, flows down, and merges into Pro. #1. As a result, the protrusion grows rapidly and becomes tongue-like in shape with a mini-keyhole on its top. Eventually, the protrusion explodes because of irregular internal thermal and pressure fluctuations and causes the ejections of melt ligaments and fast spatters (e.g., > 40 m/s in the case of Ti-6Al-4V alloy).

D. Limitations

The extreme thermal conditions in laser melting create many highly dynamic physical phenomena. A thorough understanding of them is essential for the ability to tailor microstructures and eliminate defects (Gu and Shen, 2007; Islam *et al.*, 2013; Cunningham *et al.*, 2017a; Zhao *et al.*, 2019; Pollock *et al.*, 2020; Thampy *et al.*, 2020; Todaro *et al.*, 2020; Zhao *et al.*, 2020; Martin *et al.*, 2021). However, they are too detailed and overly complex for routine process development. In reality, their collective effects, the melt pool and vapor depression morphologies, are used as the guideline (Paul and Debroy, 1988; Assuncao *et al.*, 2012; King *et al.*, 2014; Qi *et al.*, 2017; Simonds *et al.*, 2018; Cunningham *et al.*, 2019). They define the melting modes, as we now shall summarize.

III. POSTMORTEM- AND PROCESS-BASED MELTING MODES

The melting modes, as shown in Fig. 3(a), bridge laser-matter interactions and microstructures as well as defects. They ignore the physical details and focus on the macroscopic appearance of (fused) melt pool (and possibly also vapor depression). According to measurement methods, the modes can be postmortem-based or process-based. For the postmortem-based definitions, the morphology of melt pool is derived from the postmortem transverse cross-section (Paul and Debroy, 1988; Assuncao *et al.*, 2012; King *et al.*, 2014; Qi *et al.*, 2017; Scipioni Bertoli *et al.*, 2017b; Simonds *et al.*, 2018). In the process-based version, the morphologies of melt pool and vapor depression are measured directly from the *in situ* and real-time data (e.g., high-speed x-ray images) (Cunningham *et al.*, 2019; Chen *et al.*, 2020; Zhao *et al.*, 2020). With increasing temperature, the aspect ratio of (fused) melt pool (and possibly also vapor depression) in either case increases. Accordingly, the melting mode changes from conduction (via the transition) to keyhole.

A. Postmortem-based definitions

Traditionally, the melting modes are defined based on mainly practical and partially theoretical evidence (Dowden *et al.*, 1985; Kaplan, 1994; Semak and Matsunawa, 1997; Rai *et al.*, 2007; King *et al.*, 2014; Scipioni Bertoli *et al.*, 2017b). Because of the lack of effective tools to characterize the transient nature of the subsurface melt pool and vapor depression, our understanding of laser melting has relied heavily on subjective experience and simulation modeling for tens of years.

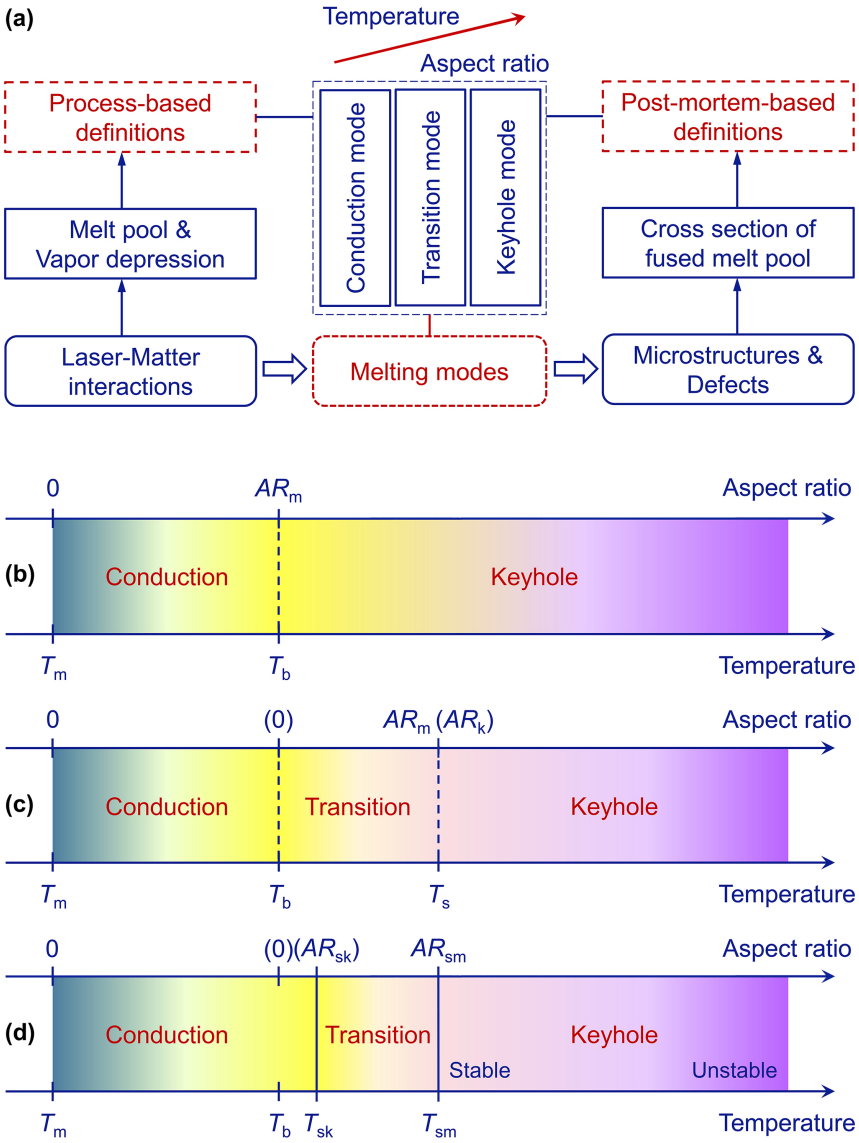

FIG. 3. Postmortem-based and process-based definitions of laser melting modes. (**a**) Basis for definitions. With increasing temperature, the depth-to-width aspect ratio of (fused) melt pool (and possibly also vapor depression) increases, and the laser melting transitions from conduction to keyhole mode. (**b-d**) Historical evolution of the definitions. (**b**) Original and (**c**) updated versions of postmortem-based definitions. (**d**) Process-based definitions. Along the axis of aspect ratio (AR), the values in the bracket are the characteristic aspect ratios of the vapor depression; otherwise, they are the characteristic aspect ratios of the (fused) melt pool. The AR_k at T_s in (**c**) and AR_{sk} at T_{sk} in (**d**) are aspect ratios where the vapor depression starts to deviate from the semicircular shape. The AR_m at T_s in (**c**) and AR_{sm} at T_{sm} in (**d**) are aspect ratios where the (fused) melt pool starts to deviate from the nearly semicircular shape.

1. Theoretical consideration

In theory, the characteristic temperature points appear as ideal thresholds that separate the melting modes, as illustrated in Figs. 3(b) and 3(c). Originally, only the boiling point (T_b) or a point below the boiling (T_c) was used [Fig. 3(b)] (Dowden *et al.*, 1985; Semak and Matsunawa, 1997; Zhao and DebRoy, 2003; Rai *et al.*, 2007; King *et al.*, 2014; Scipioni Bertoli *et al.*, 2017b; Fabbro *et al.*, 2018; Jadhav *et al.*, 2021). Below T_b or T_c, the melting is in conduction mode and conductive heat transfer largely governs the melt pool geometry (Eagar and Tsai, 1983; Kaplan, 1994; Shu *et al.*, 2021; Derimow *et al.*, 2022), while above the point, it is in keyhole mode and the melt pool morphology is mainly controlled by convective heat transfer (Semak and Matsunawa, 1997; Rai *et al.*, 2007; Bauereiß *et al.*, 2014; Khairallah *et al.*, 2016). This intuition captures some features of melt pool. For example, once the applied energy density is above a threshold, the melt pool grows rapidly in depth (King *et al.*, 2014). However, the role of vaporization, initially at least, has been greatly exaggerated. Upon boiling, the recoil pressure from the vaporization is in fact insufficient to power the fast growth of the vapor

depression as well as the melt pool (Cunningham *et al.*, 2019; Wang *et al.*, 2020). Later, a second characteristic temperature was introduced, T_s, and it is the point at which the recoil pressure starts to overcome the surface tension pressure [Fig. 3(c)] (Hirano *et al.*, 2011; Trapp *et al.*, 2017). That is, in-between the two modes, there exists a transition mode, in which conductive and convective heat transfers compete (Lee *et al.*, 2002; Assuncao *et al.*, 2012). This update closes several loopholes in the original definitions such as the occurrence of rapid vaporization prior to the keyhole mode, and the results seem to match with experimental observations (Figs. 4(b) and 4(c)). It shall be pointed out that heat convection cannot be ignored in the conduction mode to accurately describe the melt pool morphology (Shu *et al.*, 2021; Derimow *et al.*, 2022).

2. Traditional definitions

In practice, these two or three melting modes, conduction, (transition), keyhole, are often defined according to the postmortem transverse cross-section of a fused melt pool (Paul and Debroy, 1988; Assuncao *et al.*, 2012; King *et al.*, 2014; Qi *et al.*, 2017; Scipioni Bertoli *et al.*, 2017b; Patel and Vlasea, 2020). For example, in Fig. 4(a), when it is shallow, semicircular, and has a low aspect ratio (i.e., subsurface depth to width), the melting is considered to be in conduction mode; when it is deep, conical, and has a high aspect ratio, the melting is in keyhole mode (King *et al.*, 2014; Scipioni Bertoli *et al.*, 2017b). In transition mode, the cross-section is in between and may be mixed of the two sorts of shapes (Assuncao *et al.*, 2012; Qi *et al.*, 2017; Simonds *et al.*, 2018). Figure 4(b) shows the relationship between melting mode and scan velocity (Qi *et al.*, 2017). Under a scanning laser beam with constant power and spot size, as the velocity increases, the mode shifts from keyhole to transition to conduction. Similarly, Fig. 4(c) describes the melting mode transitions for a stationary laser beam (Assuncao *et al.*, 2012). For the same spot size and interaction time, with the increase in laser irradiance (*aka* power density, laser power divided by area), the aspect ratio of the cross-section in the transition mode is characterized by a plateau.

These postmortem-based definitions are simple and conceptually reasonable. They have served as guidelines to the community for decades – in metal AM, the so-called conduction mode or the very beginning of the transition mode shall be used to avoid excessive porosity (DebRoy *et al.*, 2018). Compared with the original ones, the updated definitions undoubtedly represent an improvement. However, there are no clear boundaries that separate the three modes, and the value of the plateau in Fig. 4(c) varies with laser spot size and interaction time. They have historic limitations because of the lack of direct observation of melt pool and vapor depression dynamics (e.g., morphology evolutions).

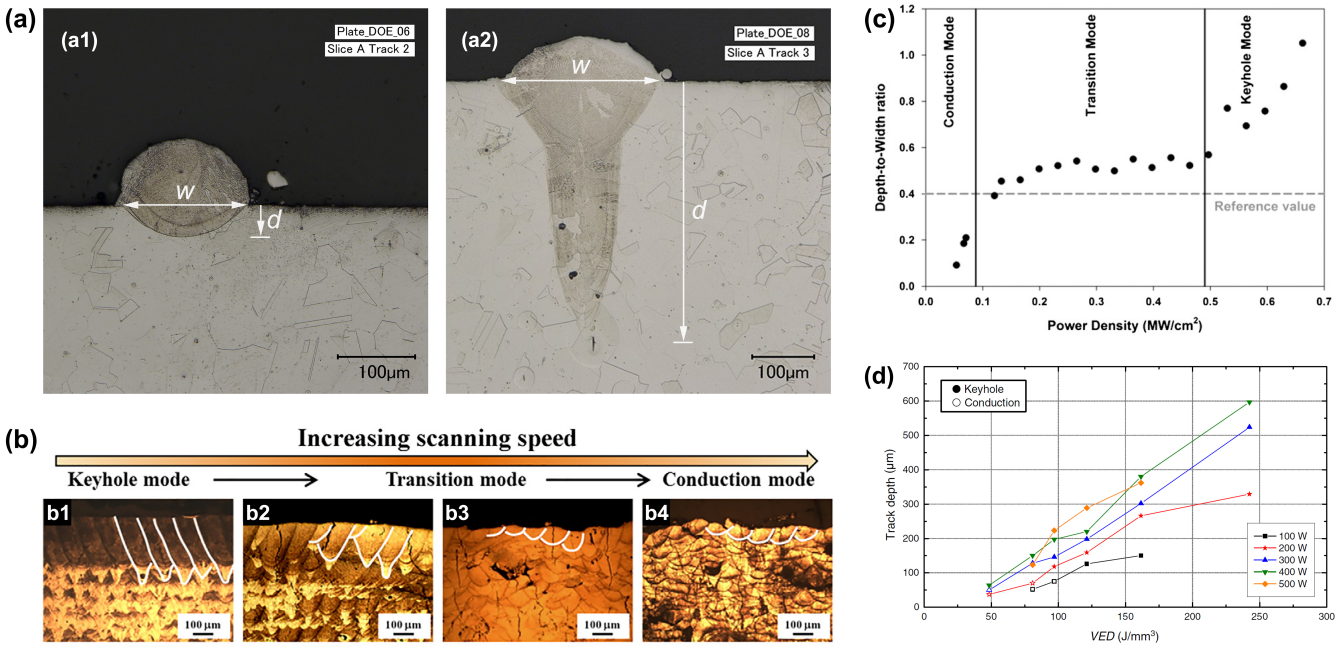

FIG. 4. Laser melting modes defined by postmortem transverse cross-sections of the fused melt pool. (**a**) Original definitions of conduction mode (a1) and keyhole mode (a2). The depth d and width w to calculate the aspect ratio are marked out in blue. (**b**) Melting mode transitions via varying scan velocity in laser powder bed fusion. (**c**) Aspect ratio of fused melt pool as a function of power density. The laser is a stationary beam, the spot size and the interaction time are constants. (**d**) Depth of fused melt pool as a function of volumetric energy density. Panels from (**a**) King *et al.*, 2014; (**b**) Qi *et al.*, 2017; (**c**) Assuncao *et al.*, 2012; (**d**) Scipioni Bertoli *et al.*, 2017b.

B. Process-based definitions

1. Conceptual definitions

The *operando* high-speed synchrotron x-ray imaging technique was first reported by Zhao *et al*. to monitor the laser fusion AM process [see Appendix A for more details] (Zhao *et al.*, 2017). With unprecedented temporal and spatial resolutions as well as high frame rates (e.g., subnanosecond, micrometer, and megahertz), orders of magnitude higher than those in laboratory x-ray imaging (Matsunawa *et al.*, 1998), the highly dynamic and transient physical processes, in particular the melt pool and vapor depression behavior below the sample surface, have been probed (Zhao *et al.*, 2017; Calta *et al.*, 2018; Leung *et al.*, 2018; Miyagi *et al.*, 2018; Parab *et al.*, 2018; Martin *et al.*, 2019b; Wolff *et al.*, 2019; Zhao *et al.*, 2019; Hocine *et al.*, 2020; Zhao *et al.*, 2022), and the definitions of laser melting modes have been revised correspondingly (Cunningham *et al.*, 2019). The results are summarized in Table I and Figs. 5(a-c). Under a stationary laser beam, the melting mode changes over time from conduction to transition to keyhole.

In conduction mode, the melt pool is stable and shows a quasi-semicircular morphology. This is consistent with traditional postmortem cross-section results (Assuncao *et al.*, 2012; King *et al.*, 2014; Qi *et al.*, 2017; Scipioni Bertoli *et al.*, 2017b). However, there may exist a shallow and semicircular vapor cavity inside the melt pool because of the high irradiance at the center of a Gaussian profiled laser beam (Cunningham *et al.*, 2019; Wang *et al.*, 2020; Wei *et al.*, 2022). This is different from pure conduction. As shown in Fig. 3(c), in the updated postmortem-based definitions, strong vaporization begins in transition mode. Meanwhile, in the definitions described here (Fig. 3(d)), the end point of conduction mode lies beyond the boiling point.

In transition mode, the melt pool maintains a stable and quasi-semicircular shape, while the vapor depression becomes deep and conical and exhibits fluctuations. This detailed information was missing from prior reports (Lee *et al.*, 2002; Assuncao *et al.*, 2012; Qi *et al.*, 2017; Tenbrock *et al.*, 2020). In the traditional understanding, it is believed that the evolutions of the melt pool and vapor depression morphologies are synchronized or that they are both quasi-semicircular in shape (Trapp *et al.*, 2017). But here, the vapor depression dynamics are much more transient than the melt pool dynamics. In Fig. 3(d), the temperature point at which the recoil pressure starts to overcome the surface tension pressure is denoted by T_{sk}, instead of T_s. It is the beginning of transition mode, not yet keyhole mode.

In keyhole mode, the melt pool is deep and narrow and may show a bimodal shape with a bowl on the top and a spike at the bottom. This is largely consistent with traditional results. The differences are two-fold: on one hand, the vapor depression, compared to the melt pool, may exhibit much stronger fluctuations (i.e., larger amplitude and higher frequency); on the other hand, in Fig. 3(d), the temperature point at which the melt pool starts to grow rapidly in the depth direction is written as T_{sm}, which is similar but not necessarily identical to the T_s in the postmortem-based definitions. In addition, the keyhole mode regime is subdivided into stable and unstable keyhole regions. In the unstable region, the instability of the vapor depression (i.e., strong fluctuation and collapse) could cause spatter ejection and pore formation (Matsunawa *et al.*, 1998; Khairallah *et al.*, 2016; Zhao *et al.*, 2017; Kiss *et al.*, 2019; Zhao *et al.*, 2019; Khairallah *et al.*, 2020; Zhao *et al.*, 2020).

Clearly, a vapor depression could exist in all three melting modes. That is, the laser beam generally does not interact with a flat melt pool directly, but through some sort of the vapor depression, either shallow or deep.

From the perspective of thermal transport, the two temperature points, T_{sk} and T_{sm}, mainly depend on local absorbed laser energy, melt flow flux, thermal diffusion flux, evaporation latent heat, solid/liquid transition latent heat, and heat loss from surface radiation and convection (Ki *et al.*, 2002; Cook and Murphy, 2020). Given a Gaussian beam, a material and a processing environment, when there exists an abrupt increase in laser absorption because of light trapping and focusing and thus in temperature and recoil pressure at the bottom of the vapor depression, the force balance on the local vapor/liquid interface is broken (Wang *et al.*, 2020; Wei *et al.*, 2022). The vapor depression then becomes unstable and grows rapidly in depth, with a conical tip (Fig. 5(b)). As the tip is close to the melt pool bottom, the large local thermal gradient causes high Marangoni force and thus violent melt flow. This transports a large amount of heat to the solid/liquid interface of the melt pool bottom, beyond the thermal regulation capacity. As a result, the melt pool becomes unstable and shows a conical or spike tip (Fig. 5(c)).

Based on the morphologies of both melt pool and vapor depression, the melting modes have been redefined (Cunningham *et al.*, 2019). Although the example in Figs. 5(a)-5(c) uses a stationary laser beam, the approach can be extended to the scanning laser case either by converting the transition times to the critical scan velocities (Fig. 5(f)) or by examining the transverse cross-sections of melt pool and vapor depression. These process-based definitions break the historic limitations and offer new community guidelines. Most of all, to a large extent, it is the vapor depression that bridges the laser beam and the melt pool in laser fusion AM of metals.

2. Strict definitions

The term “keyhole” needs to be reconsidered prior to the strict definitions of melting modes. Rather than an empirical derivation from the traditional postmortem transverse cross-

section of a fused melt pool, we prefer to redefine it directly from the morphology of the vapor-dominated cavity. When the cavity deviates from the semicircular shape, it is a keyhole. Strictly speaking, we propose that for a cavity with the width w, if some portion of the incident laser beam at the location of less than $w/4$ away from the laser beam centerline reflects more than once inside the cavity, it is a keyhole. Ray tracing, where the laser beam is represented by a collection of idealized narrow beams called rays, is a geometrical approach to calculating laser propagation and absorption (Boley *et al.*, 2015; Zhao *et al.*, 2019). In the strict keyhole definition proposed here, angle- and polarization-dependent absorptivity is not considered.

Under a stationary laser beam with a given spot size, the melting mode depends on both laser irradiance and interaction time (Assuncao *et al.*, 2012; Cunningham *et al.*, 2019). To strictly define the modes, some aspects of the physical process of laser melting (i.e., vapor depression and melt pool evolutions) are needed. That is, the interaction time, instead of the irradiance, is demonstrated here.

In Fig. 5(d), for a given laser power and spot size, the curve of vapor depression depth versus time shows a distinct transition point, before which the depth grows slowly at a nearly constant rate, and after which the depth starts to fluctuate. The transition at this time point is defined as the vapor depression transition. It strictly defines the upper limit of conduction mode and the lower limit of transition mode (Table I). Before the transition, the cavity is not a keyhole in the strict sense.

In Fig. 5(e), the depth-to-width aspect ratio of melt pool over time exhibits two distinct transitions. The first transition coincides with the vapor depression transition defined in Fig. 5(d), after which the aspect ratio increases rapidly. This coincidence indicates that the vapor depression dynamics in conduction mode, if there exists a vapor cavity, are relatively slow and the melt pool dynamics can catch up. The second transition occurs when the aspect ratio reaches a value of about 0.5 (varies with laser power), after which the increase in aspect ratio stagnates. This transition is defined as the melt pool transition, which defines the upper limit of transition mode and the lower limit of keyhole mode (Table I).

Here, two transition times are involved: one is the time to the vapor depression transition, and the other is to the melt pool transition. Both decrease rapidly with the increase in laser irradiance. This could be the physical foundation of melting modes in the laser power-scan velocity space. We note that, as indicated in Fig. 5(e), the aspect ratio of melt pool for the second transition is not constant but positively related to the irradiance. That is why, in Fig. 3(d), we state that the temperature point of T_{sm} (or the aspect ratio value of AR_{sm}) does not equal the point of T_s (or the value of AR_m) in the traditional definitions.

3. From stationary to scanning

For a given spot size, the two main processing parameters for a scanning laser beam are laser power (P) and velocity (V). They constitute the P-V space (Ion *et al.*, 1992; Kruth *et al.*, 2005; Beuth *et al.*, 2013; Gong *et al.*, 2014; Cunningham *et al.*, 2019; Scime and Beuth, 2019b; Zhao *et al.*, 2020). It is an effective but heuristic approach in laser fusion additive manufacturing to directly relate the build quality to the P-V space. In comparison to other studies that used the density or porosity or fused melt pool or mechanical strength that is postmortem-based as the metric, Figs. 5(f) and 5(g) use the transient vapor depression that is process-based. When the velocity approaches zero, the scanning beam becomes stationary. In other words, on the macro level, regardless of their differences (e.g., asymmetric melt pool and vapor depression morphologies under scanning), the stationary and the scanning are intrinsically connected via the laser-matter interaction time (Cunningham *et al.*, 2019; Zhao *et al.*, 2020).

TABLE I. Melting modes defined by high-speed x-ray imaging of stationary laser melting

Melting modes	Vapor depression transition		Melt pool transition
	Conduction mode	*Transition mode*	*Keyhole mode*
Vapor depression	✓ May exist; ✓ If exist, shallow and semicircular; ✓ Stable.	✓ Deep and conical; ✓ Fluctuation.	✓ May show strong fluctuation and collapse.
Melt pool	✓ Shallow and semicircular; ✓ Stable, and almost synchronized with the vapor depression.	✓ Semicircular; ✓ Stable.	✓ Deep and conical or bimodal (a bowl on top and a spike at bottom); ✓ Weak fluctuation.

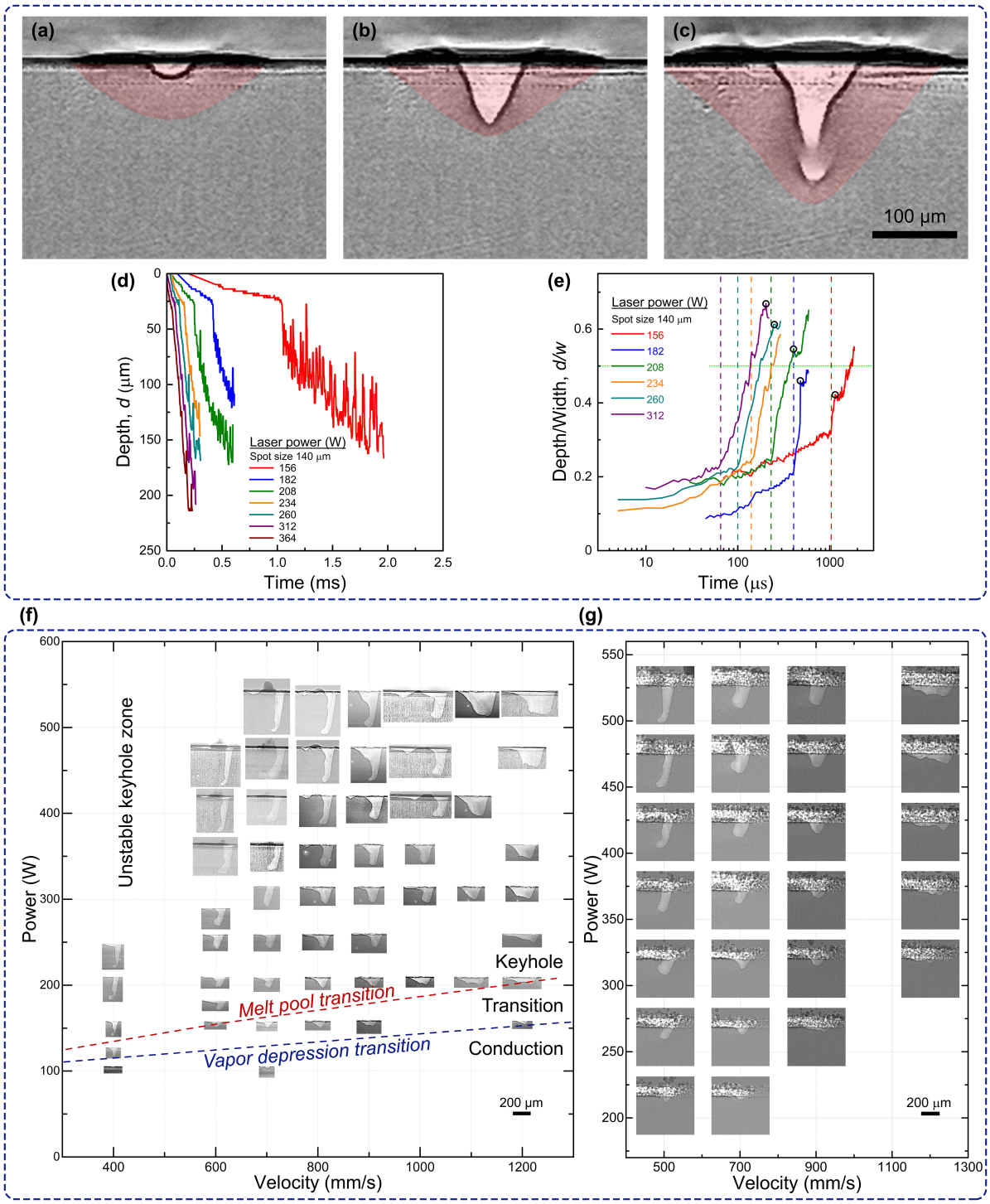

FIG. 5. Laser melting modes defined by the vapor depression and melt pool morphologies through high-speed synchrotron x-ray imaging. (**a-c**) Conceptual definitions in stationary laser melting. From left to right, it is conduction, transition, and keyhole mode, respectively. The light area is the vapor depression and the red shaded area shows the melt pool. (**d-e**) Strict definitions based on quantitative morphology measurement from (**a-c**). (**d**) Penetration depth of vapor depression and (**e**) aspect ratio of melt pool over time at various laser powers. The transitions in (**d**) and the time points indicated by the vertical dashed lines in (**e**) define the vapor depression transition. The open circles in (**e**) define the melt pool transition. (**f-g**) Extended definitions in the *P-V* space for the case of a scanning laser. (**f**) Bare plate. (**g**) Powder bed. The lower blue and upper red dashed lines in (**f**) outline the vapor depression and melt pool transitions, respectively. The laser spot size in (**f**) is 95 μm and that in (**g**) is 115 μm. Adapted from Cunningham *et al.*, 2019.

As mentioned, the melting modes defined under a stationary beam could be extended to the scanning case through the two transition time points (t_d), $V_d = D/t_d$, where D is the laser spot size. For a given laser power, there are two critical velocity points corresponding to the vapor depression and melt pool transitions, respectively. For a series of powers, these points could be connected to two lines, dividing the *P-V* space into conduction, transition, and keyhole regimes. As shown in Fig. 5(f), the lower blue line is for the vapor depression transition, and the upper red is for the melt pool transition. Additionally, the keyhole regime could be further classified into stable and unstable regions, and the latter corresponds to the high-power and low-velocity area in the *P-V* space.

As for the role of powder in laser powder bed fusion AM, note that the stable keyhole morphology (as well as the melting mode) follows the same trend regardless of the presence of powder [Figs. 5(f) and 5(g)] (Cunningham *et al.*, 2019). This accords with the general observation that the presence of powder makes little difference to the melt pool size, for example. Later, the teams at the Lawrence Livermore National Laboratory and the University of California Santa Barbara also claimed that the details of the powder become far less important when the power is above a certain value (Khairallah *et al.*, 2020; Polonsky and Pollock, 2020). Most recently, the role of powder around the keyhole porosity regime is statistically analyzed, and the results show that the addition of powder increases the keyhole instability but only slightly widens the porosity regime in the *P-V* space (Zhao *et al.*, 2020). An additional effect of the powder is that the gas atomized powder typically contains porosity some fraction of which may be inherited (Aboulkhair *et al.*, 2014; Cunningham *et al.*, 2017b; Iebba *et al.*, 2017).

According to the extended definitions in Figs. 5(f) and 5(g), nearly all the *P-V* combinations, including those commonly used in commercial laser powder bed fusion AM machines, are in the transition or keyhole mode. This is surprising. To some extent, it shows why it is always extremely challenging to eliminate keyhole pores (not formed at laser turn points or caused by imperfect powder spreading) when the machines are operated in the supposed conduction mode (Cunningham *et al.*, 2017a; Martin *et al.*, 2019a; Zhao *et al.*, 2020).

These extended definitions of melting modes in the *P-V* space are not strict, particularly in the low-power and low-velocity region where the vapor depression and melt pool fluctuations are significant. They are simply derived from the stationary laser measurements and are good for very basic evaluations. This is consistent with the fact that the parameter of applied energy density has limitations for precise quantification of the melt pool depth as well as the melting mode [Fig. 4(d)] (Prashanth *et al.*, 2017; Scipioni Bertoli *et al.*, 2017b). This may be attributed to the large variation in the vapor depression morphology across the space (Figs. 5(f) and 5(g)), which can significantly alter the laser absorption through multiple, angle-dependent absorption events. This in turn affects the melt flow hydrodynamics through Marangoni convection, recoil pressure, and vapor impact, and ultimately the melt pool morphology (Kouraytem *et al.*, 2019).

In practice, the melting modes under a scanning laser beam can be defined according to the transverse cross-sections of melt pool and vapor depression. This may be assisted by the three-dimensional multiphysics simulations after model calibration and validation using high-speed synchrotron x-ray imaging data (Kouraytem *et al.*, 2019; Khairallah *et al.*, 2020; Wang *et al.*, 2020; Gan *et al.*, 2021; Wei *et al.*, 2022), which resembles those under a stationary beam (Figs. 5(a)-5(e) and Table I). For example, when the vapor depression deviates from semicircular, the laser melting enters the transition mode. Under the low-power and low-scan-velocity laser conditions, the vapor depression may appear as extremely narrow (much smaller than the laser spot size) and high-aspect-ratio. The main reasons are three-fold. First, the laser absorption increases because of multiple reflections. Second, the edge of the low-power Gaussian beam cannot provide sufficient energy to vaporize the metal. Third, the laser melting may transition from conduction to stable-keyhole to unstable-keyhole mode during a scan because of variations in local material or laser conditions such as sample preheating or surface oxidization ahead of the laser beam or powder motion and shading above the surface (Rubenchik *et al.*, 2014; Yang *et al.*, 2018; Martin *et al.*, 2019b; Khairallah *et al.*, 2020; Zhao *et al.*, 2020).

IV. GAPS IN KNOWLEDGE AND OPPORTUNITIES

A. Emerging knowledge

A few key points of the process-based definitions are summarized here. Firstly, there exists a potential for vapor depression formation in all three modes, and beyond the conduction mode, the vapor depression dynamics are much more transient than the melt pool dynamics. Secondly, under stationary laser melting, the two time nodes corresponding to the vapor depression and melt pool transitions strictly define the three melting modes. Thirdly, the melting modes in the stationary laser melting could be extended to the scanning case, according to which, commercial AM machines are typically operated in either transition or stable keyhole mode. However, similar to the case of using applied energy density as a measure, caution should be exercised because of the large variations in the vapor depression morphology and laser absorption across the *P-V* space. Alternatively, the modes under a scanning beam could be defined by the transverse cross-sections of melt pool and vapor depression. The multiphysics simulations after model calibration and validation play an essential role in connecting the longitudinal and transverse cross-sections of vapor depression and melt pool as well as deriving the process-based definitions from

the postmortem evidence by providing three-dimensional structure information (Rai *et al.*, 2007; Kouraytem *et al.*, 2019; Khairallah *et al.*, 2020; Wang *et al.*, 2020; Gan *et al.*, 2021; Wei *et al.*, 2022).

B. Beyond x-ray imaging

The *operando* high-speed synchrotron x-ray imaging has been an invaluable tool for probing the laser fusion process. In addition to direct measurement, the melt pool and vapor depression morphology evolutions could be translated into other signal forms such as dynamic laser absorption, vapor plume dynamics, and ultrasound signals for the mode definitions through, as shown in Fig. 6, combining high-speed x-ray imaging and other *in situ* and real-time monitoring techniques such as integrating sphere radiometry (Khairallah *et al.*, 2021; Simonds *et al.*, 2021), schlieren imaging (Bidare *et al.*, 2018; Bitharas *et al.*, 2022), and immersion ultrasound (Gillespie *et al.*, 2021). These could be feasible and efficient approaches for process monitoring where in-process x-ray imaging is not an option (Zhao *et al.*, 2022). To facilitate the translations (also between the *in situ* and *ex situ* data), physics-based modeling, big data approach and appropriate experimental design are the keys (Scime and Beuth, 2019b; Shevchik *et al.*, 2019; Zhang *et al.*, 2019; Gan *et al.*, 2021; Zhu *et al.*, 2021b).

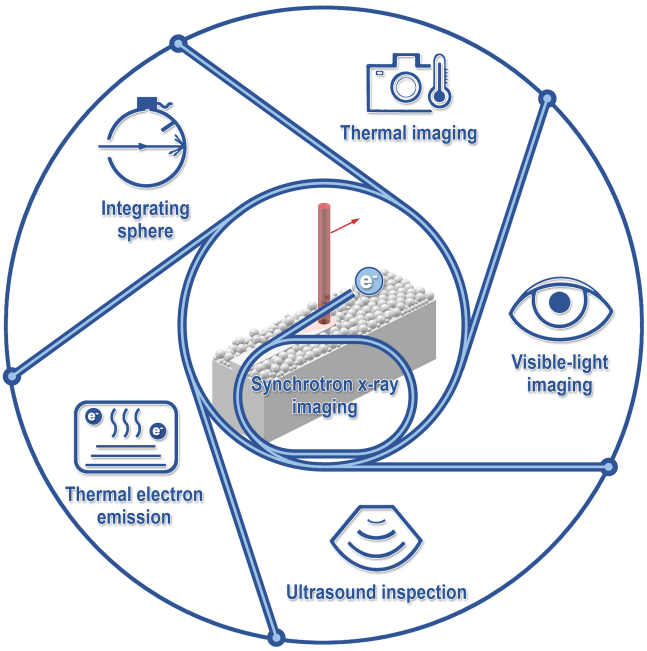

FIG. 6. Integration of *operando* synchrotron x-ray imaging and other high-speed *in-situ* monitoring techniques. Through multi-technique fusion and multi-signal translation, the emerging knowledge obtained from synchrotron x-rays can be transferred to industrial practice.

For example, a team at the National Institute of Standards and Technology combined integrating sphere radiometry and high-speed x-ray imaging and correlated the laser absorption with the vapor depression evolution and melting modes (Simonds *et al.*, 2021). The energy absorbed by the sample during the laser melting process is calculated from the energy balance of the incident light and the absolute reflected light measured by the spheres (Fabbro *et al.*, 2006; Norris and Robino, 2008). It is found that the energy absorption increases sharply when the laser melting enters into the transition mode from the conduction mode, drops upon the decrease of the vapor depression depth (Simonds *et al.*, 2021), and periodically fluctuates when the probability of forming a transient keyhole pore increases (Simonds *et al.*, 2020; Khairallah *et al.*, 2021). These correlations along with the very high temporal resolution and readily processable one-dimensional datastream make absolute absorption an appealing approach for process-based melt pool monitoring.

Immersion ultrasound was also performed simultaneously with high-speed x-ray imaging to monitor the melt pool and vapor depression dynamics (Gillespie *et al.*, 2021). The basic principle of the ultrasound technique is that the amplitude of the scattered waveform is a result of local variations in elastic properties and mass density (Schmerr Jr., 2016; Shevchik *et al.*, 2018). In this study, the time of flight of the ultrasound scattering from the melt pool was found to be highly sensitive to the depth of the melt pool (Gillespie *et al.*, 2021). This technique in principle could be implemented in the industrial-scale additive manufacturing process. However, more research effort is needed because of the complex nature of the ultrasonic signal itself.

C. Stable-keyhole AM

These process-based definitions offer new guidelines to the AM community. One direct conclusion is that, in laser powder bed fusion AM of metals, a stable keyhole region is desirable to achieve full-density builds. Compared to the stable keyhole region, the transition region is much smaller. Together they outline the process window for a metallic material, as illustrated in Fig. 7(a). Outside of the window, the *P-V* space is occupied by several zones that potentially create microstructural defects or dimensional inaccuracy, e.g., keyhole porosity, balling, and lack-of-fusion porosity (Chandrasekhar, 1981; Tolochko *et al.*, 2004; Gu and Shen, 2007; Amara and Fabbro, 2010; Tang *et al.*, 2017; DebRoy *et al.*, 2018; Scime and Beuth, 2019b; Snow *et al.*, 2020; Zhao *et al.*, 2020; DebRoy *et al.*, 2021; Gan *et al.*, 2021; Laleh *et al.*, 2021; Sanaei and Fatemi, 2021; Zhu *et al.*, 2021a; Huang *et al.*, 2022; Mostafaei *et al.*, 2022). To take full advantage of this window, we need to confirm and understand its boundaries. In practice, these boundaries are often approached as process engineers strive to increase build times or as local variations in build conditions (e.g., laser spot size, scan velocity, air flow, powder bed surface) create

momentary deviations from prescribed *P-V* parameters. In other words, there is a need to uncover the fundamental origins of those defects. As an example in Fig. 7(b-c) (Zhao *et al.*, 2020), it is discovered through high-speed synchrotron x-ray imaging that the keyhole porosity boundary is smooth and sharp. Only when pores near the keyhole tip obtain sufficient kinetic energy from the acoustic waves (high-amplitude, short-duration, and depth-oriented) released from the critical keyhole instability (in analogy with a double palm strike in the artwork) could they escape rapidly from the large thermal gradient field around the keyhole and become trapped by the solidification front as defects. This acoustic-wave-driven mechanism is distinct from the viscous-drag-driven mechanism, which requires sufficient waiting time created by the retracting keyhole (Bayat *et al.*, 2019; Zhao *et al.*, 2020).

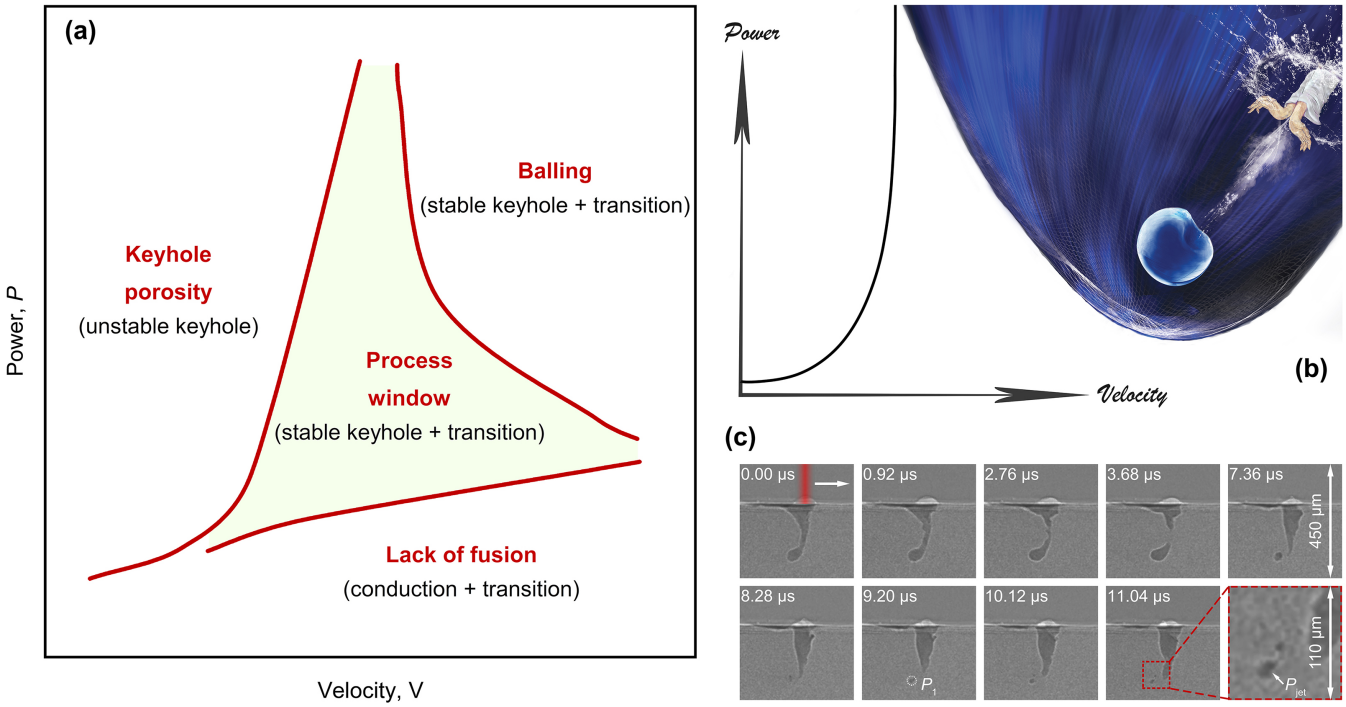

FIG. 7. Schematic diagrams of process map for laser powder bed fusion of metals. (**a**) Process window. The process window locates at the center of the *P-V* space and is surrounded by several common defect zones. The definitions of melting modes here are process-based. Only part of the mixing stable-keyhole and transition region constitutes the window. At low energy density (low power and high scan velocity), balling can extend the region of lack-of-fusion porosity by causing variability in melt pool size, and thus, the overlapping area between the "balling" and "lack of fusion" regions is designated to the latter. (**b-c**) Boundary and origin of keyhole porosity. (**b**) Artwork showing the keyhole porosity boundary and origin. On the left side of the figure, the keyhole porosity boundary in the *P-V* space is sharp and smooth. On the right side, around the porosity boundary, the critical keyhole instability that is analogous to a double palm strike emits an acoustic wave (shock wave) and drives the pore near the keyhole tip to accelerate rapidly away from the keyhole. When the pore is captured by the solidification front, it becomes a detrimental structural defect in the build. (**c**) X-ray images of keyhole pore formation and motion around the keyhole porosity boundary. In the first few μs after a pore pinches off the keyhole, the original keyhole tip keeps nearly stationary. The pore P_1 that is marked by a dashed circle is then accelerated to about 10 m/s in less than 1 μs. At time 11.04 μs, a microjet (P_{jet}, see the figure inset) is penetrating into the pore P_1 from the side facing the keyhole bottom. The x-ray images are background corrected and the contrast is then reversed to highlight the events around the keyhole. Figure (**c**) adapted from Zhao *et al.*, 2020.

From another perspective, in comparison to conduction-mode AM, the stable-keyhole-mode AM is more energy-efficient, sustainable, and robust. Firstly, it avoids lack-of-fusion porosity from incomplete melting of powder particles, though it is crucial to note that this defect source is dominated by insufficient melt pool overlap (and is thus another example where energy density is inadequate as a metric) (Tang *et al.*, 2017; Gordon *et al.*, 2020). Secondly, the laser beam undergoes multiple reflections inside the keyhole, which enhances laser absorption and improves energy efficiency (Trapp *et al.*, 2017; Simonds *et al.*, 2018; Allen *et al.*, 2020), particularly for those highly reflective metals such as aluminum, copper, gold, and their alloys (Buchbinder *et al.*, 2011; Boley *et al.*, 2015; Ikeshoji *et al.*, 2018; Jadhav *et al.*, 2021). Thirdly, the keyhole attracts, captures, and removes nearby pores from various sources like the powder and

surfaces because of thermocapillary force (Selva *et al.*, 2010; Brennen, 2013; Hojjatzadeh *et al.*, 2019; Leung *et al.*, 2019; Zhao *et al.*, 2020). Fourthly, a stable keyhole tends to maintain its morphology and depth over time, having no distinct protrusions on the front keyhole wall, and some changes in the laser and powder conditions will generally not disturb the stability (Cunningham *et al.*, 2019; Kouraytem *et al.*, 2019; Wang *et al.*, 2020; Zhao *et al.*, 2020; Gan *et al.*, 2021). This expands the process window. Additionally, the mechanical and corrosion properties of the build could be strengthened as a result of the refining of grain and phase structures (Roehling *et al.*, 2020; Lu *et al.*, 2021).

D. Process metrology

A significant need for improved process metrology exists in laser fusion AM of metals (Slotwinski and Garboczi, 2015; Mani *et al.*, 2017). The most relevant of these for accurate determination of melting modes are laser power, beam profile, and scan velocity (Hu and Mahadevan, 2017; Williams *et al.*, 2017). Together, they determine the amount of energy delivered at any location during a build. For laser power, traditional thermal power meters are readily available with uncertainties typically in the range of 3 % to 5 % (Williams *et al.*, 2021). However, such uncertainties are not often reported in the literature and the laser power is assumed to be what was requested by the user. The physics-based definitions offered above point to the importance of laser irradiance in determining the melting modes. For the accurate determination of transferrable process windows, we recommend that laser power be directly measured, and uncertainties stated, for every study that considers power as a variable.

The beam profile is also very important for determining the melt pool outcomes, as has been shown with simulations (Yan *et al.*, 2020). In the literature, the generic term "spot size" is often simply stated. A single parameter like this can be used only if the geometric profile of the beam is known (to some uncertainty) and its definition explicitly stated (e.g., $1/e^2$, $1/e$). Several commercial systems are currently available for measuring beam profile, but there is no method of establishing absolute traceability as there is with laser power, which presents a metrology opportunity whereby discrepancies between commercial beam profilers could be quantified and resolved.

Lastly, scan velocity plays an equally important role in determining dwell time and thus the energy delivered during a laser scan. Nonetheless, little attention has been paid to its measurement or accuracy.

V. CONCLUSION

In this review, we have described the general physical process of laser melting. It is the complex interplay of many physical mechanisms caused by extreme thermal conditions that determines the vapor depression and melt pool morphologies and defines the melting mode. The melting mode changes with increasing temperature from conduction to transition to keyhole.

According to the morphology measurement approaches, the definitions of melting modes can be postmortem- or process-based. The postmortem-based definitions are conceptually reasonable but they are subjective, vague, and confusing because of the omission of the vapor depression details. By contrast, the process-based definitions, where the morphologies of both melt pool and vapor depression are measured directly from the *operando* high-speed x-ray images, are clearer and more complete. They solve the mystery of keyhole pores generated in the traditionally defined conduction mode.

The revision of the melting mode definitions suggests new guidelines and directions. Firstly, in laser fusion AM of metals, the laser-matter interactions are mainly with a vapor cavity. Beyond the conduction mode, the vapor depression is much more dynamic and transient than traditionally anticipated. Secondly, the stable-keyhole laser melting proposes an approach for sustainable and robust additive manufacturing. The boundaries and origins of some common defect generation zones in the *P*-*V* space are still lacking. In addition, multiphysics simulations, signal translations from morphology data to other feasible and complementary measurement signals, and improved process metrology are being used to develop transferrable process windows across platforms and scales.

Briefly, it is the *operando* high-speed x-ray imaging technique that opens a door to the physical process underlying the laser melting a few decades after the concept of keyholing was first proposed. With the technical advancement, it is possible to re-examine the long-standing problems at higher spatial, temporal, and energy resolutions and continue to update or revise the existing theories and models. Here, we hope this short review will not only deepen the understanding of laser melting modes but also inspire the mind in frontier research and development of laser fusion additive manufacturing of metals.

LIST OF SYMBOLS AND ABBREVIATIONS

AR: aspect ratio

AR_k: aspect ratio of vapor depression that defines the lower limit of keyhole mode in the updated version of the postmortem-based definitions

AR_m: aspect ratio of melt pool that defines the lower limit of keyhole mode in the original version of the postmortem-based definitions

AR_{sk}: aspect ratio of vapor depression that defines the lower limit of transition mode in the process-based definitions

AR_{sm}: aspect ratio of melt pool that defines the lower limit of keyhole mode in the process-based definitions

d: depth of a postmortem transverse cross-section of the fused melt pool or a vapor depression

D: spot size of laser beam

P: laser power

t: time

t_d: time point of the vapor depression or melt pool transition

T: peak temperature of melt pool

T_b: boiling point

T_c: a temperature below the boiling point that defines the lower limit of keyhole mode in the original version of the postmortem-based definitions

T_m: melting point

T_s: peak temperature of melt pool at which the aspect ratio of melt pool reaches AR_m in the updated version of the postmortem-based definitions

T_{sk}: peak temperature of melt pool at which the aspect ratio of vapor depression reaches AR_{sk} in the process-based definitions

T_{sm}: peak temperature of melt pool at which the aspect ratio of melt pool reaches AR_{sm} in the process-based definitions

V: laser scan velocity

V_d: critical velocity point of the vapor depression or melt pool transition

w: width of a postmortem transverse cross-section of the fused melt pool or a vapor depression

aka: also known as

AM: additive manufacturing

APS: Advanced Photon Source

BCC: Body-centered cubic

DLF: direct laser fabrication

DLS: Diamond Light Source

ESRF: European Synchrotron Radiation Facility

FCC: Face-centered cubic

LENS: laser engineered net shaping

LPBF: laser powder bed fusion

Pro.: protrusion structure on the front keyhole wall

Pro.$^+$: protrusion structure tilting upward on the front keyhole wall

Pro.$^-$: protrusion structure leaning downward on the front keyhole wall

RP: rapid prototyping

RTS: reverse-triangle-like shape, describing a transient state of the keyhole bottom

SLS: Swiss Light Source

SPring-8: Super Photon ring-8 GeV

SSRL: Stanford Synchrotron Radiation Lightsource

Subs.: metal substrate

ACKNOWLEDGMENTS

CZ, BS (Bo Shi) and SC acknowledge support from the National Natural Science Foundation of China (52175332), the Tsinghua-Imperial Research and Innovation Seed Fund, and the startup fund of Tsinghua University. DD acknowledges support from the National Natural Science Foundation of China (U1537205). TS acknowledges the start-up fund from the University of Virginia. ADR acknowledges support from NASA's University Leadership Initiative (ULI) program under grant 80NSSC19M0123. We are grateful to N. Parab, L. Chen, W. Tan, S. Wolff, X. Li, Q. Guo, B. Gould, N. Kouraytem, R. Cunningham, I. Bitharas, C.M. Kube, and F.D. Carlo for stimulating collaborations. We thank N. Derimow and O.L. Kafka of the National Institute of Standards and Technology (NIST) for their careful review and feedback on this manuscript. We also thank F. Lin, H. Xie, A. Godfrey, and B. Chang at Tsinghua University for fruitful discussions. We are grateful to Y. Huang and Y. Feng for assistance with the artworks in Figs 6 and 7(b). Synchrotron experiments in this contribution used resources of the Advanced Photon Source, a U.S. Department of Energy (DOE) Office of Science User Facility operated for the DOE Office of Science by Argonne National Laboratory under contract no. DE-AC02-06CH11357.

APPENDIX A: HIGH-SPEED SYNCHROTRON X-RAY IMAGING

The *operando* high-speed synchrotron x-ray imaging results of laser melting shown in Figs. 2 and 5 were obtained from a home-built experimental apparatus at the 32-ID-B beamline of the Advanced Photon Source (APS) at Argonne National Laboratory (Zhao *et al.*, 2017; Parab *et al.*, 2018; Zhao *et al.*, 2022). As shown in Fig. 8, it consists of an x-ray imaging system and a laser powder bed fusion simulator.

Generally, a short-period undulator (18 mm) with a gap of 12 mm to 14 mm is used to generate polychromatic x-rays with the integrated flux of ~7×10^{15} ph/s and the first harmonic energy at ~24 keV (Fezzaa and Wang, 2008; Wang *et al.*, 2008; Hudspeth *et al.*, 2015). The imaging system includes a 100 μm thick Lu3Al5O12:Ce scintillator, a 45° reflection mirror, a 10× objective lens (NA = 0.28, Edmund Optics Inc., USA), a tube lens, and a Photron FastCam SA-Z camera (Fig. 5, Photron Inc., Japan) or a Shimadzu HPV-X2 camera (Fig. 2, Shimadzu Corp., Japan).[1] The spatial resolution is 2 μm/pixel to 3 μm/pixel, the minimum effective exposure time for each x-ray image is a single x-ray pulse (~100 ps), and the maximum effective frame rate is 6.5 million frames per second.

In a typical laser melting experiment, a powder bed sample, which is made of two identical pieces of glassy

carbon (vitreous) plates, one metal base, and one layer of metal powder, is loaded into a custom-built vacuum chamber, with the sample thickness along the x-ray direction and the thickness centerline on the laser scanning plane (Zhao *et al.*, 2017). The sample thickness needs to be optimized to well image the real fusion process. In practice, a series of samples having various thicknesses from hundreds of microns to a few millimeters should be used to confirm that the keyhole morphology and depth under the given laser conditions have no detectable difference between the chosen sample and the bulkier sample. Then, the chamber is pumped down and purged with pure argon gas back to atmospheric pressure. The laser heating system consists of an ytterbium fiber laser (IPG YLR-500-AC, USA) and a galvo laser scanner (intelliSCANde 30, SCANLAB GmbH, Germany).[1] The fiber laser is in single mode, providing pure Gaussian beam profiles. The wavelength and the maximum laser power are 1,070 nm and 560 W, respectively. With a f/340 mm objective lens and a f/85 mm collimator, the laser beam spot size is 50 μm ± 5 μm ($1/e^2$) at the focal plane. The actual spot size on the sample surface is controlled by defocusing. The scan speed of the scanner at the focal plane could reach 2.0 m/s.

During the experiment, the laser is often operated in continuous-wave mode and scans along a single straight line to heat the metal sample. Simultaneously, the x-ray beam penetrates through the sample and provides a side view of the laser melting through both absorption and phase contrasts (Wilkins *et al.*, 1996; Fezzaa and Wang, 2008; Wang *et al.*, 2008), from which the melt pool and vapor depression morphologies could be identified and measured.

In addition to the APS, intensive research activities at other synchrotron facilities have been conducted around the world during past years to study the metal additive manufacturing process such as Diamond Light Source (DLS), Stanford Synchrotron Radiation Lightsource (SSRL), European Synchrotron Radiation Facility (ESRF), Super Photon ring-8 GeV (SPring-8), and Swiss Light Source (SLS) (Calta *et al.*, 2018; Leung *et al.*, 2018; Miyagi *et al.*, 2018; Martin *et al.*, 2019b; Hocine *et al.*, 2020). They have largely promoted the fundamental understanding of various physical phenomena, microstructures, and defects in laser fusion of metals.

[1] Certain commercial equipment, instruments, and/or materials are identified in this paper to specify the experimental procedure. Such identification does not imply recommendation or endorsement by the National Institute of Standards and Technology.

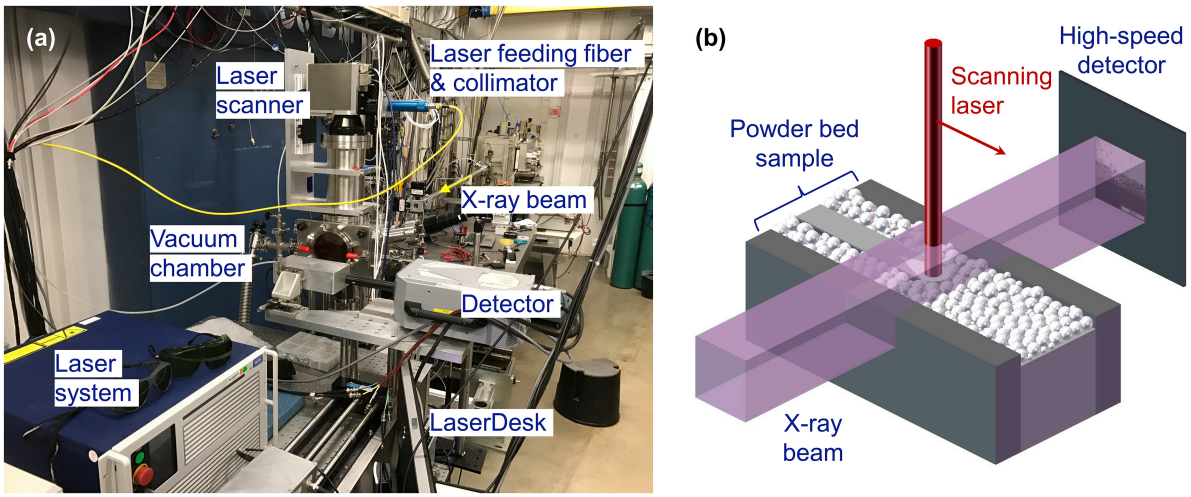

FIG. 8. Synchrotron x-ray imaging of laser melting. (**a**) Configuration of experimental systems. (**b**) Experimental schematic.

REFERENCES

Aboulkhair, N. T., N. M. Everitt, I. Ashcroft, and C. Tuck, 2014, "Reducing porosity in AlSi10Mg parts processed by selective laser melting," Additive Manufacturing **1-4**, 77-86.

Aboulkhair, N. T., I. Maskery, C. Tuck, I. Ashcroft, and N. M. Everitt, 2016, "On the formation of AlSi10Mg single tracks and layers in selective laser melting: Microstructure and nano-mechanical properties," Journal of Materials Processing Technology **230**, 88-98.

Agrawal, P., S. Thapliyal, S. S. Nene, R. S. Mishra, B. A. McWilliams, and K. C. Cho, 2020, "Excellent strength-ductility synergy in metastable high entropy alloy by laser powder bed additive manufacturing," Additive Manufacturing **32**, 101098.

Allen, T. R., W. Huang, J. R. Tanner, W. Tan, J. M. Fraser, and B. J. Simonds, 2020, "Energy-coupling mechanisms revealed through simultaneous keyhole depth and absorptance measurements during laser-metal processing," Physical Review Applied **13**, 064070.

Amara, E. H., and R. Fabbro, 2010, "Modeling of humps formation during deep-penetration laser welding," Applied Physics A **101**, 111-116.

Anisimov, S. I., and V. A. Khokhlov, 1995, *Instabilities in laser-matter interaction* (CRC press).

Assuncao, E., S. Williams, and D. Yapp, 2012, "Interaction time and beam diameter effects on the conduction mode limit," Optics and Lasers in Engineering **50**, 823-828.

Atwood, C., M. Griffith, L. Harwell, E. Schlienger, M. Ensz, J. Smugeresky, T. Romero, D. Greene, and D. Reckaway, 1998, "Laser engineered net shaping (LENS™): A tool for direct fabrication of metal parts," International Congress on Applications of Lasers & Electro-Optics **1998**, E1-E7.

Bauereiß, A., T. Scharowsky, and C. Körner, 2014, "Defect generation and propagation mechanism during additive manufacturing by selective beam melting," Journal of Materials Processing Technology **214**, 2522-2528.

Bayat, M., A. Thanki, S. Mohanty, A. Witvrouw, S. Yang, J. Thorborg, N. S. Tiedje, and J. H. Hattel, 2019, "Keyhole-induced porosities in laser-based powder bed fusion (L-PBF) of Ti6Al4V: High-fidelity modelling and experimental validation," Additive Manufacturing **30**, 100835.

Beuth, J. L., J. Fox, J. Gockel, C. Montgomery, R. Yang, H. Qiao, E. Soylemez, P. Reeseewatt, A. Anvari, S. P. Narra*, et al.*, 2013, "Process mapping for qualification across multiple direct metal additive manufacturing processes," in *2013 International Solid Freeform Fabrication Symposium*, University of Texas at Austin, p. 655-665.

Bidare, P., I. Bitharas, R. Ward, M. Attallah, and A. J. Moore, 2018, "Fluid and particle dynamics in laser powder bed fusion," Acta Materialia **142**, 107-120.

Bitharas, I., N. Parab, C. Zhao, T. Sun, A. D. Rollett, and A. J. Moore, 2022, "The interplay between vapour, liquid, and solid phases in laser powder bed fusion," Nature Communications **13**, 2959.

Boettinger, W. J., D. Shechtman, R. J. Schaefer, and F. S. Biancaniello, 1984, "The effect of rapid solidification velocity on the microstructure of Ag-Cu alloys," Metallurgical Transactions A **15**, 55-66.

Boley, C. D., S. A. Khairallah, and A. M. Rubenchik, 2015, "Calculation of laser absorption by metal powders in additive manufacturing," Appl. Opt. **54**, 2477-2482.

Bontha, S., N. W. Klingbeil, P. A. Kobryn, and H. L. Fraser, 2006, "Thermal process maps for predicting solidification microstructure in laser fabrication of thin-wall structures," Journal of Materials Processing Technology **178**, 135-142.

Brennen, C. E., 2013, *Cavitation and bubble dynamics* (Cambridge University Press, Cambridge).

Brika, S. E., M. Letenneur, C. A. Dion, and V. Brailovski, 2020, "Influence of particle morphology and size distribution on the powder flowability and laser powder bed fusion manufacturability of Ti-6Al-4V alloy," Additive Manufacturing **31**, 100929.

Brown, M. S., and C. B. Arnold, 2010, in *Fundamentals of laser-material interaction and application to multiscale surface modification,* edited by Sugioka, K., M. Meunier, and A. Piqué (Springer Berlin Heidelberg, Berlin, Heidelberg), p. 91-120.

Buchbinder, D., H. Schleifenbaum, S. Heidrich, W. Meiners, and J. Bültmann, 2011, "High power selective laser melting (HP SLM) of aluminum parts," Physics Procedia **12**, 271-278.

Calta, N. P., J. Wang, A. M. Kiss, A. A. Martin, P. J. Depond, G. M. Guss, V. Thampy, A. Y. Fong, J. N. Weker, K. H. Stone*, et al.*, 2018, "An instrument for *in situ* time-resolved X-ray imaging and diffraction of laser powder bed fusion additive manufacturing processes," Review of Scientific Instruments **89**, 055101.

Campbell, F. C., 2008, *Elements of metallurgy and engineering alloys* (ASM International).

Campbell, I., D. Bourell, and I. Gibson, 2012, "Additive manufacturing: rapid prototyping comes of age," Rapid Prototyping Journal **18**, 255-258.

Chandrasekhar, S., 1981, *Hydrodynamic and hydromagnetic stability* (Dover Publications, New York).

Chen, Y., S. J. Clark, C. L. A. Leung, L. Sinclair, S. Marussi, M. P. Olbinado, E. Boller, A. Rack, I. Todd, and P. D. Lee, 2020, "In-situ synchrotron imaging of keyhole mode multi-layer laser powder bed fusion additive manufacturing," Applied Materials Today **20**, 100650.

Chiang, P.-J., R. Jiang, R. Cunningham, N. Parab, C. Zhao, K. Fezzaa, T. Sun, and A. D. Rollett, 2019, "In situ characterization of hot cracking using dynamic X-ray radiography," in *Advanced Real Time Imaging II*, Cham, edited by Nakano, J., P. C. Pistorius, C. Tamerler, H. Yasuda, Z. Zhang, N. Dogan, W. Wang, N. Saito, and B. Webler (Springer International Publishing), p. 77-85.

Cho, J.-H., and S.-J. Na, 2006, "Implementation of real-time multiple reflection and Fresnel absorption of laser beam in keyhole," Journal of Physics D: Applied Physics **39**, 5372-5378.

Cook, P. S., and A. B. Murphy, 2020, "Simulation of melt pool behaviour during additive manufacturing: Underlying physics and progress," Additive Manufacturing **31**, 100909.

Cunningham, R., S. P. Narra, C. Montgomery, J. Beuth, and A. D. Rollett, 2017a, "Synchrotron-based X-ray microtomography characterization of the effect of processing variables on porosity formation in laser powder-bed additive manufacturing of Ti-6Al-4V," JOM **69**, 479-484.

Cunningham, R., S. P. Narra, T. Ozturk, J. Beuth, and A. D. Rollett, 2016, "Evaluating the effect of processing parameters

on porosity in electron beam melted Ti-6Al-4V via synchrotron X-ray microtomography," JOM **68**, 765-771.

Cunningham, R., A. Nicolas, J. Madsen, E. Fodran, E. Anagnostou, M. D. Sangid, and A. D. Rollett, 2017b, "Analyzing the effects of powder and post-processing on porosity and properties of electron beam melted Ti-6Al-4V," Materials Research Letters **5**, 516-525.

Cunningham, R., C. Zhao, N. Parab, C. Kantzos, J. Pauza, K. Fezzaa, T. Sun, and A. D. Rollett, 2019, "Keyhole threshold and morphology in laser melting revealed by ultrahigh-speed x-ray imaging," Science **363**, 849-852.

Daeneke, T., K. Khoshmanesh, N. Mahmood, I. A. de Castro, D. Esrafilzadeh, S. J. Barrow, M. D. Dickey, and K. Kalantar-zadeh, 2018, "Liquid metals: fundamentals and applications in chemistry," Chemical Society Reviews **47**, 4073-4111.

DebRoy, T., T. Mukherjee, H. L. Wei, J. W. Elmer, and J. O. Milewski, 2021, "Metallurgy, mechanistic models and machine learning in metal printing," Nature Reviews Materials **6**, 48-68.

DebRoy, T., H. Wei, J. Zuback, T. Mukherjee, J. Elmer, J. Milewski, A. M. Beese, A. Wilson-Heid, A. De, and W. Zhang, 2018, "Additive manufacturing of metallic components–process, structure and properties," Progress in Materials Science **92**, 112-224.

Derimow, N., E. J. Schwalbach, J. T. Benzing, J. P. Killgore, A. B. Artusio-Glimpse, N. Hrabe, and B. J. Simonds, 2022, "In situ absorption synchrotron measurements, predictive modeling, microstructural analysis, and scanning probe measurements of laser melted Ti-6Al-4V single tracks for additive manufacturing applications," Journal of Alloys and Compounds **900**, 163494.

Doubenskaia, M., M. Pavlov, S. Grigoriev, and I. Smurov, 2013, "Definition of brightness temperature and restoration of true temperature in laser cladding using infrared camera," Surface and Coatings Technology **220**, 244-247.

Dowden, J., 2017, in *Laser keyhole welding: The vapour phase,* edited by Dowden, J., and W. Schulz (Springer International Publishing, Cham), p. 113-151.

Dowden, J., M. Davis, and P. Kapadia, 1985, "The flow of heat and the motion of the weld pool in penetration welding with a laser," Journal of Applied Physics **57**, 4474-4479.

Dowling, L., J. Kennedy, S. O'Shaughnessy, and D. Trimble, 2020, "A review of critical repeatability and reproducibility issues in powder bed fusion," Materials & Design **186**, 108346.

Eagar, T., and N. Tsai, 1983, "Temperature fields produced by traveling distributed heat sources," Welding journal **62**, 346-355.

El-Sayed, M. A., 2001, "Some Interesting Properties of Metals Confined in Time and Nanometer Space of Different Shapes," Accounts of Chemical Research **34**, 257-264.

Elmer, J. W., P. W. Hochanadel, K. Lachenberg, C. Caristan, and T. Webber, 2011, in *Introduction to high energy density electron and laser beam welding,* edited by Lienert, T., T. Siewert, S. Babu, and V. Acoff (ASM International), p. 507-513.

Fabbro, R., and K. Chouf, 2000, "Keyhole modeling during laser welding," Journal of Applied Physics **87**, 4075-4083.

Fabbro, R., M. Dal, P. Peyre, F. Coste, M. Schneider, and V. Gunenthiram, 2018, "Analysis and possible estimation of keyhole depths evolution, using laser operating parameters and material properties," Journal of Laser Applications **30**, 032410.

Fabbro, R., S. Slimani, I. Doudet, F. Coste, and F. Briand, 2006, "Experimental study of the dynamical coupling between the induced vapour plume and the melt pool for Nd–Yag CW laser welding," Journal of Physics D: Applied Physics **39**, 394-400.

Farshidianfar, M. H., A. Khajepour, and A. P. Gerlich, 2016, "Effect of real-time cooling rate on microstructure in laser additive manufacturing," Journal of Materials Processing Technology **231**, 468-478.

Fezzaa, K., and Y. Wang, 2008, "Ultrafast X-ray phase-contrast imaging of the initial coalescence phase of two water droplets," Physical Review Letters **100**, 104501.

Forien, J.-B., N. P. Calta, P. J. DePond, G. M. Guss, T. T. Roehling, and M. J. Matthews, 2020, "Detecting keyhole pore defects and monitoring process signatures during laser powder bed fusion: A correlation between *in situ* pyrometry and *ex situ* X-ray radiography," Additive Manufacturing **35**, 101336.

Foroozmehr, A., M. Badrossamay, E. Foroozmehr, and S. i. Golabi, 2016, "Finite element simulation of selective laser melting process considering optical penetration depth of laser in powder bed," Materials & Design **89**, 255-263.

Frazier, W. E., 2014, "Metal additive manufacturing: A review," Journal of Materials Engineering and Performance **23**, 1917-1928.

Gan, Z., O. L. Kafka, N. Parab, C. Zhao, L. Fang, O. Heinonen, T. Sun, and W. K. Liu, 2021, "Universal scaling laws of keyhole stability and porosity in 3D printing of metals," Nature Communications **12**, 2379.

Gäumann, M., S. Henry, F. Cléton, J. D. Wagnière, and W. Kurz, 1999, "Epitaxial laser metal forming: analysis of microstructure formation," Materials Science and Engineering: A **271**, 232-241.

Gaynor, A. T., and J. K. Guest, 2016, "Topology optimization considering overhang constraints: Eliminating sacrificial

support material in additive manufacturing through design," Structural and Multidisciplinary Optimization **54**, 1157-1172.

Gillespie, J., W. Y. Yeoh, C. Zhao, N. D. Parab, T. Sun, A. D. Rollett, B. Lan, and C. M. Kube, 2021, "*In situ* characterization of laser-generated melt pools using synchronized ultrasound and high-speed X-ray imaging," The Journal of the Acoustical Society of America **150**, 2409-2420.

Gisario, A., M. Kazarian, F. Martina, and M. Mehrpouya, 2019, "Metal additive manufacturing in the commercial aviation industry: A review," Journal of Manufacturing Systems **53**, 124-149.

Gong, H., K. Rafi, H. Gu, T. Starr, and B. Stucker, 2014, "Analysis of defect generation in Ti–6Al–4V parts made using powder bed fusion additive manufacturing processes," Additive Manufacturing **1-4**, 87-98.

Gordon, J. V., S. P. Narra, R. W. Cunningham, H. Liu, H. Chen, R. M. Suter, J. L. Beuth, and A. D. Rollett, 2020, "Defect structure process maps for laser powder bed fusion additive manufacturing," Additive Manufacturing **36**, 101552.

Griffith, M. L., D. M. Keicher, C. L. Atwood, J. A. Romero, J. E. Smugeresky, L. D. Harwell, and D. L. Greene, 1996, "Free Form Fabrication of Metallic Components using Laser Engineered Net Shaping (LENS™)," in *1996 Solid Freeform Fabrication Symposium*, University of Texas at Austin, p. 125–132.

Griffith, M. L., M. E. Schlienger, L. D. Harwell, M. S. Oliver, M. D. Baldwin, M. T. Ensz, M. Essien, J. Brooks, C. V. Robino, J. E. Smugeresky*, et al.*, 1999, "Understanding thermal behavior in the LENS process," Materials & Design **20**, 107-113.

Gu, D., and Y. Shen, 2007, "Balling phenomena during direct laser sintering of multi-component Cu-based metal powder," Journal of Alloys and Compounds **432**, 163-166.

Gu, D., X. Shi, R. Poprawe, D. L. Bourell, R. Setchi, and J. Zhu, 2021, "Material-structure-performance integrated laser-metal additive manufacturing," Science **372**, eabg1487.

Guo, Q., C. Zhao, L. I. Escano, Z. Young, L. Xiong, K. Fezzaa, W. Everhart, B. Brown, T. Sun, and L. Chen, 2018, "Transient dynamics of powder spattering in laser powder bed fusion additive manufacturing process revealed by in-situ high-speed high-energy x-ray imaging," Acta Materialia **151**, 169-180.

Gur, C. H., and J. Pan, 2008, *Handbook of thermal process modeling steels* (CRC Press).

Gusarov, A. V., and I. Smurov, 2010, "Modeling the interaction of laser radiation with powder bed at selective laser melting," Physics Procedia **5**, 381-394.

Heiden, M. J., L. A. Deibler, J. M. Rodelas, J. R. Koepke, D. J. Tung, D. J. Saiz, and B. H. Jared, 2019, "Evolution of 316L stainless steel feedstock due to laser powder bed fusion process," Additive Manufacturing **25**, 84-103.

Heigel, J. C., B. M. Lane, and L. E. Levine, 2020, "In situ measurements of melt-pool length and cooling rate during 3d builds of the metal am-bench artifacts," Integrating Materials and Manufacturing Innovation **9**, 31-53.

Herzog, D., V. Seyda, E. Wycisk, and C. Emmelmann, 2016, "Additive manufacturing of metals," Acta Materialia **117**, 371-392.

Hirano, K., R. Fabbro, and M. Muller, 2011, "Experimental determination of temperature threshold for melt surface deformation during laser interaction on iron at atmospheric pressure," Journal of Physics D: Applied Physics **44**, 435402.

Hocine, S., H. Van Swygenhoven, S. Van Petegem, C. S. T. Chang, T. Maimaitiyili, G. Tinti, D. Ferreira Sanchez, D. Grolimund, and N. Casati, 2020, "Operando X-ray diffraction during laser 3D printing," Materials Today **34**, 30-40.

Hojjatzadeh, S. M. H., N. D. Parab, Q. Guo, M. Qu, L. Xiong, C. Zhao, L. I. Escano, K. Fezzaa, W. Everhart, T. Sun*, et al.*, 2020, "Direct observation of pore formation mechanisms during LPBF additive manufacturing process and high energy density laser welding," International Journal of Machine Tools and Manufacture **153**, 103555.

Hojjatzadeh, S. M. H., N. D. Parab, W. Yan, Q. Guo, L. Xiong, C. Zhao, M. Qu, L. I. Escano, X. Xiao, K. Fezzaa*, et al.*, 2019, "Pore elimination mechanisms during 3D printing of metals," Nature Communications **10**, 3088.

Hooper, P. A., 2018, "Melt pool temperature and cooling rates in laser powder bed fusion," Additive Manufacturing **22**, 548-559.

Hossain, M. S., J. A. Gonzalez, R. M. Hernandez, M. A. I. Shuvo, J. Mireles, A. Choudhuri, Y. Lin, and R. B. Wicker, 2016, "Fabrication of smart parts using powder bed fusion additive manufacturing technology," Additive Manufacturing **10**, 58-66.

Hou, J., B. Dai, Y. Li, J. Zhao, Z. Chen, D. Pan, Y. Zhu, K. Zhang, and A. Huang, 2020, "Helium bubble nucleation in Laser Powder Bed Fusion processed 304L stainless steel," Journal of Nuclear Materials **542**, 152443.

Hu, Y. N., S. C. Wu, P. J. Withers, J. Zhang, H. Y. X. Bao, Y. N. Fu, and G. Z. Kang, 2020, "The effect of manufacturing defects on the fatigue life of selective laser melted Ti-6Al-4V structures," Materials & Design **192**, 108708.

Hu, Z., and S. Mahadevan, 2017, "Uncertainty quantification and management in additive manufacturing: current status, needs, and opportunities," The International Journal of Advanced Manufacturing Technology **93**, 2855-2874.

Huang, Y., T. G. Fleming, S. J. Clark, S. Marussi, K. Fezzaa, J. Thiyagalingam, C. L. A. Leung, and P. D. Lee, 2022, "Keyhole fluctuation and pore formation mechanisms during

laser powder bed fusion additive manufacturing," Nature Communications **13**, 1170.

Hudspeth, M., T. Sun, N. Parab, Z. Guo, K. Fezzaa, S. Luo, and W. Chen, 2015, "Simultaneous X-ray diffraction and phase-contrast imaging for investigating material deformation mechanisms during high-rate loading," Journal of Synchrotron Radiation **22**, 49-58.

Iebba, M., A. Astarita, D. Mistretta, I. Colonna, M. Liberini, F. Scherillo, C. Pirozzi, R. Borrelli, S. Franchitti, and A. Squillace, 2017, "Influence of powder characteristics on formation of porosity in additive manufacturing of Ti-6Al-4V components," Journal of Materials Engineering and Performance **26**, 4138-4147.

Ikeshoji, T.-T., K. Nakamura, M. Yonehara, K. Imai, and H. Kyogoku, 2018, "Selective laser melting of pure copper," JOM **70**, 396-400.

Ion, J. C., H. R. Shercliff, and M. F. Ashby, 1992, "Diagrams for laser materials processing," Acta metallurgica et materialia **40**, 1539-1551.

Islam, M., T. Purtonen, H. Piili, A. Salminen, and O. Nyrhilä, 2013, "Temperature profile and imaging analysis of laser additive manufacturing of stainless steel," Physics Procedia **41**, 835-842.

ISO/ASTM 52900-15, 2015, in (ASTM International, West Conshohocken, PA).

Jadhav, S. D., L. R. Goossens, Y. Kinds, B. V. Hooreweder, and K. Vanmeensel, 2021, "Laser-based powder bed fusion additive manufacturing of pure copper," Additive Manufacturing **42**, 101990.

Joint Defense Manufacturing Council, 2021, "Department of Defense additive manufacturing strategy".

Juhasz, M., R. Tiedemann, G. Dumstorff, J. Walker, A. D. Plessis, B. Conner, W. Lang, and E. MacDonald, 2020, "Hybrid directed energy deposition for fabricating metal structures with embedded sensors," Additive Manufacturing **35**, 101397.

Kaplan, A., 1994, "A model of deep penetration laser welding based on calculation of the keyhole profile," Journal of Physics D: Applied Physics **27**, 1805.

Kenel, C., D. Grolimund, X. Li, E. Panepucci, V. A. Samson, D. F. Sanchez, F. Marone, and C. Leinenbach, 2017, "In situ investigation of phase transformations in Ti-6Al-4V under additive manufacturing conditions combining laser melting and high-speed micro-X-ray diffraction," Scientific Reports **7**, 16358.

Khairallah, S. A., A. T. Anderson, A. Rubenchik, and W. E. King, 2016, "Laser powder-bed fusion additive manufacturing: Physics of complex melt flow and formation mechanisms of pores, spatter, and denudation zones," Acta Materialia **108**, 36-45.

Khairallah, S. A., A. A. Martin, J. R. I. Lee, G. Guss, N. P. Calta, J. A. Hammons, M. H. Nielsen, K. Chaput, E. Schwalbach, M. N. Shah*, et al.*, 2020, "Controlling interdependent meso-nanosecond dynamics and defect generation in metal 3D printing," Science **368**, 660.

Khairallah, S. A., T. Sun, and B. J. Simonds, 2021, "Onset of periodic oscillations as a precursor of a transition to pore-generating turbulence in laser melting," Additive Manufacturing Letters **1**, 100002.

Ki, H., J. Mazumder, and P. S. Mohanty, 2002, "Modeling of laser keyhole welding: Part I. mathematical modeling, numerical methodology, role of recoil pressure, multiple reflections, and free surface evolution," Metallurgical and Materials Transactions A **33**, 1817-1830.

King, W., A. Anderson, R. Ferencz, N. Hodge, C. Kamath, S. Khairallah, and A. Rubenchik, 2015, "Laser powder bed fusion additive manufacturing of metals; physics, computational, and materials challenges," Applied Physics Reviews **2**, 041304.

King, W. E., H. D. Barth, V. M. Castillo, G. F. Gallegos, J. W. Gibbs, D. E. Hahn, C. Kamath, and A. M. Rubenchik, 2014, "Observation of keyhole-mode laser melting in laser powder-bed fusion additive manufacturing," Journal of Materials Processing Technology **214**, 2915-2925.

Kiss, A. M., A. Y. Fong, N. P. Calta, V. Thampy, A. A. Martin, P. J. Depond, J. Wang, M. J. Matthews, R. T. Ott, C. J. Tassone*, et al.*, 2019, "Laser-induced keyhole defect dynamics during metal additive manufacturing," Advanced Engineering Materials **21**, 1900455.

Kosonen, T., K. Kakko, and N. Raitanen, 2021, "Evaluation of pore re-opening after HIP in LPBF Ti–6Al–4V," Powder Metallurgy **64**, 425-433.

Kouraytem, N., X. Li, R. Cunningham, C. Zhao, N. Parab, T. Sun, A. D. Rollett, A. D. Spear, and W. Tan, 2019, "Effect of laser-matter interaction on molten pool flow and keyhole dynamics," Physical Review Applied **11**, 064054.

Kroos, J., U. Gratzke, and G. Simon, 1993, "Towards a self-consistent model of the keyhole in penetration laser beam welding," Journal of physics D: Applied physics **26**, 474.

Kruth, J. P., L. Froyen, J. Van Vaerenbergh, P. Mercelis, M. Rombouts, and B. Lauwers, 2004, "Selective laser melting of iron-based powder," Journal of Materials Processing Technology **149**, 616-622.

Kruth, J. P., M. C. Leu, and T. Nakagawa, 1998, "Progress in Additive Manufacturing and Rapid Prototyping," CIRP Annals **47**, 525-540.

Kruth, J. P., P. Mercelis, J. Van Vaerenbergh, L. Froyen, and M. Rombouts, 2005, "Binding mechanisms in selective laser sintering and selective laser melting," Rapid Prototyping Journal **11**, 26-36.

Kurpjuweit, S., C. G. Schmidt, M. Klöckner, and S. M. Wagner, 2021, "Blockchain in Additive Manufacturing and its Impact on Supply Chains," Journal of Business Logistics **42**, 46-70.

Kurz, W., B. Giovanola, and R. Trivedi, 1986, "Theory of microstructural development during rapid solidification," Acta Metallurgica **34**, 823-830.

Kyo, M., E. Hiyazaki, S. Tsukioka, H. Ochi, Y. Amitani, T. Tsuchiya, T. Aoki, and S. Takagawa, 1995, "The sea trial of "KAIKO", the full ocean depth research ROV," in *'Challenges of Our Changing Global Environment'. Conference Proceedings. OCEANS '95 MTS/IEEE*, p. 1991-1996.

Laleh, M., A. E. Hughes, S. Yang, J. Wang, J. Li, A. M. Glenn, W. Xu, and M. Y. Tan, 2021, "A critical insight into lack-of-fusion pore structures in additively manufactured stainless steel," Additive Manufacturing **38**, 101762.

Leach, R. K., D. Bourell, S. Carmignato, A. Donmez, N. Senin, and W. Dewulf, 2019, "Geometrical metrology for metal additive manufacturing," CIRP Annals **68**, 677-700.

Lee, J. Y., S. H. Ko, D. F. Farson, and C. D. Yoo, 2002, "Mechanism of keyhole formation and stability in stationary laser welding," Journal of Physics D: Applied Physics **35**, 1570-1576.

Leung, C. L. A., S. Marussi, R. C. Atwood, M. Towrie, P. J. Withers, and P. D. Lee, 2018, "In situ X-ray imaging of defect and molten pool dynamics in laser additive manufacturing," Nature Communications **9**, 1355.

Leung, C. L. A., S. Marussi, M. Towrie, R. C. Atwood, P. J. Withers, and P. D. Lee, 2019, "The effect of powder oxidation on defect formation in laser additive manufacturing," Acta Materialia **166**, 294-305.

Lewis, G. K., R. Nemec, J. Milewski, D. J. Thoma, D. Cremers, and M. Barbe, 1994, "Directed light fabrication," International Congress on Applications of Lasers & Electro-Optics **1994**, 17-26.

Lewis, G. K., and E. Schlienger, 2000, "Practical considerations and capabilities for laser assisted direct metal deposition," Materials & Design **21**, 417-423.

Li, X., C. Zhao, T. Sun, and W. Tan, 2020, "Revealing transient powder-gas interaction in laser powder bed fusion process through multi-physics modeling and high-speed synchrotron x-ray imaging," Additive Manufacturing **35**, 101362.

Lide, D. R., 2004, *CRC handbook of chemistry and physics* (CRC press).

Lin, S., Z. Gan, J. Yan, and G. J. Wagner, 2020, "A conservative level set method on unstructured meshes for modeling multiphase thermo-fluid flow in additive manufacturing processes," Computer Methods in Applied Mechanics and Engineering **372**, 113348.

Link, S., C. Burda, M. B. Mohamed, B. Nikoobakht, and M. A. El-Sayed, 1999, "Laser photothermal melting and fragmentation of gold nanorods: Energy and laser pulse-width dependence," The Journal of Physical Chemistry A **103**, 1165-1170.

Liu, D.-R., S. Wang, and W. Yan, 2020, "Grain structure evolution in transition-mode melting in direct energy deposition," Materials & Design **194**, 108919.

Liu, S., and Y. C. Shin, 2019, "Additive manufacturing of Ti6Al4V alloy: A review," Materials & Design **164**, 107552.

Lorazo, P., L. J. Lewis, and M. Meunier, 2003, "Short-pulse laser ablation of solids: from phase explosion to fragmentation," Physical Review Letters **91**, 225502.

Lu, J., X. Lin, N. Kang, Y. Cao, Q. Wang, and W. Huang, 2021, "Keyhole mode induced simultaneous improvement in strength and ductility of Sc modified Al–Mn alloy manufactured by selective laser melting," Materials Science and Engineering: A **811**, 141089.

Ly, S., A. M. Rubenchik, S. A. Khairallah, G. Guss, and M. J. Matthews, 2017, "Metal vapor micro-jet controls material redistribution in laser powder bed fusion additive manufacturing," Scientific reports **7**, 4085.

MacDonald, E., and R. Wicker, 2016, "Multiprocess 3D printing for increasing component functionality," Science **353**, aaf2093.

Maconachie, T., M. Leary, B. Lozanovski, X. Zhang, M. Qian, O. Faruque, and M. Brandt, 2019, "SLM lattice structures: Properties, performance, applications and challenges," Materials & Design **183**, 108137.

Mani, M., B. M. Lane, M. A. Donmez, S. C. Feng, and S. P. Moylan, 2017, "A review on measurement science needs for real-time control of additive manufacturing metal powder bed fusion processes," International Journal of Production Research **55**, 1400-1418.

Markl, M., and C. Körner, 2016, "Multiscale modeling of powder bed–based additive manufacturing," Annual Review of Materials Research **46**, 93-123.

Martin, A. A., N. P. Calta, J. A. Hammons, S. A. Khairallah, M. H. Nielsen, R. M. Shuttlesworth, N. Sinclair, M. J. Matthews, J. R. Jeffries, T. M. Willey*, et al.*, 2019a, "Ultrafast dynamics of laser-metal interactions in additive manufacturing alloys captured by *in situ* X-ray imaging," Materials Today Advances **1**, 100002.

Martin, A. A., N. P. Calta, S. A. Khairallah, J. Wang, P. J. Depond, A. Y. Fong, V. Thampy, G. M. Guss, A. M. Kiss, and K. H. Stone, 2019b, "Dynamics of pore formation during laser powder bed fusion additive manufacturing," Nature Communications **10**, 1987.

Martin, A. A., J. A. Hammons, H. B. Henderson, N. P. Calta, M. H. Nielsen, C. C. Cook, J. Ye, A. A. Maich, N. E. Teslich, T. T. Li*, et al.*, 2021, "Enhanced mechanical performance via laser induced nanostructure formation in an additively manufactured lightweight aluminum alloy," Applied Materials Today **22**, 100972.

Martin, J. H., B. D. Yahata, J. M. Hundley, J. A. Mayer, T. A. Schaedler, and T. M. Pollock, 2017, "3D printing of high-strength aluminium alloys," Nature **549**, 365–369.

Matsunawa, A., J.-D. Kim, N. Seto, M. Mizutani, and S. Katayama, 1998, "Dynamics of keyhole and molten pool in laser welding," Journal of laser applications **10**, 247-254.

McEnerney, B., R. P. Dillon, J. Vickers, K. M. Taminger, S. D. Jolly, and A. Rollett, 2021, "Enabling new science mission capabilities with additive manufacturing technologies," Bulletin of the American Astronomical Society **53**, 466.

Miller, K. J., and T. Takenaka, 1964, *Electron beam welding* (Welding Research Council Bulletin, New York).

Miotello, A., and R. Kelly, 1999, "Laser-induced phase explosion: new physical problems when a condensed phase approaches the thermodynamic critical temperature," Applied Physics A **69**, S67-S73.

Miyagi, M., Y. Kawahito, H. Wang, H. Kawakami, T. Shoubu, and M. Tsukamoto, 2018, "X-ray phase contrast observation of solidification and hot crack propagation in laser spot welding of aluminum alloy," Optics Express **26**, 22626-22636.

Mohr, M., R. Wunderlich, R. Novakovic, E. Ricci, and H.-J. Fecht, 2020, "Precise Measurements of Thermophysical Properties of Liquid Ti–6Al–4V (Ti64) Alloy On Board the International Space Station," Advanced Engineering Materials **22**, 2000169.

Mostafaei, A., C. Zhao, Y. He, S. Reza Ghiaasiaan, B. Shi, S. Shao, N. Shamsaei, Z. Wu, N. Kouraytem, T. Sun*, et al.*, 2022, "Defects and anomalies in powder bed fusion metal additive manufacturing," Current Opinion in Solid State and Materials Science **26**, 100974.

Norris, J. T., and C. V. Robino, 2008, "Development of a time resolved energy absorption measurement technique for laser beam spot welds," International Congress on Applications of Lasers & Electro-Optics **2008**, P149.

Onuike, B., B. Heer, and A. Bandyopadhyay, 2018, "Additive manufacturing of Inconel 718—Copper alloy bimetallic structure using laser engineered net shaping (LENS™)," Additive Manufacturing **21**, 133-140.

Panwisawas, C., B. Perumal, R. M. Ward, N. Turner, R. P. Turner, J. W. Brooks, and H. C. Basoalto, 2017, "Keyhole formation and thermal fluid flow-induced porosity during laser fusion welding in titanium alloys: Experimental and modelling," Acta Materialia **126**, 251-263.

Panwisawas, C., Y. T. Tang, and R. C. Reed, 2020, "Metal 3D printing as a disruptive technology for superalloys," Nature Communications **11**, 2327.

Parab, N. D., C. Zhao, R. Cunningham, L. I. Escano, K. Fezzaa, W. Everhart, A. D. Rollett, L. Chen, and T. Sun, 2018, "Ultrafast X-ray imaging of laser–metal additive manufacturing processes," Journal of Synchrotron Radiation **25**, 1467-1477.

Patel, S., and M. Vlasea, 2020, "Melting modes in laser powder bed fusion," Materialia **9**, 100591.

Paul, A., and T. Debroy, 1988, "Free surface flow and heat transfer in conduction mode laser welding," Metallurgical Transactions B **19**, 851-858.

Pollock, T. M., A. J. Clarke, and S. S. Babu, 2020, "Design and tailoring of alloys for additive manufacturing," Metallurgical and Materials Transactions A **51**, 6000-6019.

Polonsky, A. T., W. C. Lenthe, M. P. Echlin, V. Livescu, G. T. Gray, and T. M. Pollock, 2020, "Solidification-driven orientation gradients in additively manufactured stainless steel," Acta Materialia **183**, 249-260.

Polonsky, A. T., and T. M. Pollock, 2020, "Closing the science gap in 3D metal printing," Science **368**, 583-584.

Pordzik, R., and P. Woizeschke, 2020, "An experimental approach for the direct measurement of temperatures in the vicinity of the keyhole front wall during deep-penetration laser welding," Appl. Sci. **10**, 3951.

Prashanth, K. G., S. Scudino, T. Maity, J. Das, and J. Eckert, 2017, "Is the energy density a reliable parameter for materials synthesis by selective laser melting?," Materials Research Letters **5**, 386-390.

Qi, T., H. Zhu, H. Zhang, J. Yin, L. Ke, and X. Zeng, 2017, "Selective laser melting of Al7050 powder: Melting mode transition and comparison of the characteristics between the keyhole and conduction mode," Materials & Design **135**, 257-266.

Rai, R., J. Elmer, T. Palmer, and T. DebRoy, 2007, "Heat transfer and fluid flow during keyhole mode laser welding of tantalum, Ti–6Al–4V, 304L stainless steel and vanadium," Journal of physics D: Applied physics **40**, 5753.

Ramirez-San-Juan, J. C., E. Rodriguez-Aboytes, A. E. Martinez-Canton, O. Baldovino-Pantaleon, A. Robledo-Martinez, N. Korneev, and R. Ramos-Garcia, 2010, "Time-resolved analysis of cavitation induced by CW lasers in absorbing liquids," Optics Express **18**, 8735-8742.

Roehling, T. T., R. Shi, S. A. Khairallah, J. D. Roehling, G. M. Guss, J. T. McKeown, and M. J. Matthews, 2020, "Controlling grain nucleation and morphology by laser beam shaping in metal additive manufacturing," Materials & Design **195**, 109071.

Rubenchik, A., S. Wu, V. K. Kanz, M. LeBlanc, W. H. Lowdermilk, M. Rotter, and J. Stanley, 2014, "Temperature-dependent 780-nm laser absorption by engineering grade aluminum, titanium, and steel alloy surfaces," Optical Engineering **53**, 122506.

Sames, W. J., F. List, S. Pannala, R. R. Dehoff, and S. S. Babu, 2016, "The metallurgy and processing science of metal additive manufacturing," International Materials Reviews **61**, 315-360.

Sanaei, N., and A. Fatemi, 2021, "Defects in additive manufactured metals and their effect on fatigue performance: A state-of-the-art review," Progress in Materials Science **117**, 100724.

Schmerr Jr., L. W., 2016, "Fundamentals of ultrasonic nondestructive evaluation: A modeling approach," Fundamentals of Ultrasonic Nondestructive Evaluation.

Scime, L., and J. Beuth, 2019a, "Melt pool geometry and morphology variability for the Inconel 718 alloy in a laser powder bed fusion additive manufacturing process," Additive Manufacturing **29**, 100830.

Scime, L., and J. Beuth, 2019b, "Using machine learning to identify in-situ melt pool signatures indicative of flaw formation in a laser powder bed fusion additive manufacturing process," Additive Manufacturing **25**, 151-165.

Scipioni Bertoli, U., G. Guss, S. Wu, M. J. Matthews, and J. M. Schoenung, 2017a, "In-situ characterization of laser-powder interaction and cooling rates through high-speed imaging of powder bed fusion additive manufacturing," Materials & Design **135**, 385-396.

Scipioni Bertoli, U., A. J. Wolfer, M. J. Matthews, J.-P. R. Delplanque, and J. M. Schoenung, 2017b, "On the limitations of volumetric energy density as a design parameter for selective laser melting," Materials & Design **113**, 331-340.

Seltzman, A. H., and S. J. Wukitch, 2021, "Resolution and geometric limitations in laser powder bed fusion additively manufactured GRCop-84 structures for a lower hybrid current drive launcher," Fusion Engineering and Design **173**, 112847.

Selva, B., V. Miralles, I. Cantat, and M.-C. Jullien, 2010, "Thermocapillary actuation by optimized resistor pattern: bubbles and droplets displacing, switching and trapping," Lab on a Chip **10**, 1835-1840.

Semak, V., and A. Matsunawa, 1997, "The role of recoil pressure in energy balance during laser materials processing," Journal of Physics D: Applied Physics **30**, 2541-2552.

Shevchik, S. A., C. Kenel, C. Leinenbach, and K. Wasmer, 2018, "Acoustic emission for in situ quality monitoring in additive manufacturing using spectral convolutional neural networks," Additive Manufacturing **21**, 598-604.

Shevchik, S. A., G. Masinelli, C. Kenel, C. Leinenbach, and K. Wasmer, 2019, "Deep learning for *in situ* and real-time quality monitoring in additive manufacturing using acoustic emission," IEEE Transactions on Industrial Informatics **15**, 5194-5203.

Shu, Y., D. Galles, O. A. Tertuliano, B. A. McWilliams, N. Yang, W. Cai, and A. J. Lew, 2021, "A critical look at the prediction of the temperature field around a laser-induced melt pool on metallic substrates," Scientific Reports **11**, 12224.

Simonds, B. J., J. Sowards, J. Hadler, E. Pfeif, B. Wilthan, J. Tanner, C. Harris, P. Williams, and J. Lehman, 2018, "Time-resolved absorptance and melt pool dynamics during intense laser irradiation of a metal," Physical Review Applied **10**, 044061.

Simonds, B. J., J. Tanner, A. Artusio-Glimpse, P. A. Williams, N. Parab, C. Zhao, and T. Sun, 2020, "Simultaneous high-speed x-ray transmission imaging and absolute dynamic absorptance measurements during high-power laser-metal processing," Procedia CIRP **94**, 775-779.

Simonds, B. J., J. Tanner, A. Artusio-Glimpse, P. A. Williams, N. Parab, C. Zhao, and T. Sun, 2021, "The causal relationship between melt pool geometry and energy absorption measured in real time during laser-based manufacturing," Applied Materials Today **23**, 101049.

Sing, S. L., J. An, W. Y. Yeong, and F. E. Wiria, 2016, "Laser and electron-beam powder-bed additive manufacturing of metallic implants: A review on processes, materials and designs," Journal of Orthopaedic Research **34**, 369-385.

Sing, S. L., S. Huang, G. D. Goh, G. L. Goh, C. F. Tey, J. H. K. Tan, and W. Y. Yeong, 2021, "Emerging metallic systems for additive manufacturing: *In-situ* alloying and multi-metal processing in laser powder bed fusion," Progress in Materials Science **119**, 100795.

Slotwinski, J. A., and E. J. Garboczi, 2015, "Metrology needs for metal additive manufacturing powders," JOM **67**, 538-543.

Snow, Z., A. R. Nassar, and E. W. Reutzel, 2020, "Invited Review Article: Review of the formation and impact of flaws in powder bed fusion additive manufacturing," Additive Manufacturing **36**, 101457.

Sofinowski, K. A., S. Raman, X. Wang, B. Gaskey, and M. Seita, 2021, "Layer-wise engineering of grain orientation (LEGO) in laser powder bed fusion of stainless steel 316L," Additive Manufacturing **38**, 101809.

Sun, S.-H., T. Ishimoto, K. Hagihara, Y. Tsutsumi, T. Hanawa, and T. Nakano, 2019, "Excellent mechanical and corrosion properties of austenitic stainless steel with a unique crystallographic lamellar microstructure via selective laser melting," Scripta Materialia **159**, 89-93.

Tan, W., N. S. Bailey, and Y. C. Shin, 2013, "Investigation of keyhole plume and molten pool based on a three-dimensional dynamic model with sharp interface formulation," Journal of Physics D: Applied Physics **46**, 055501.

Tang, M., P. C. Pistorius, and J. L. Beuth, 2017, "Prediction of lack-of-fusion porosity for powder bed fusion," Additive Manufacturing **14**, 39-48.

Tenbrock, C., F. G. Fischer, K. Wissenbach, J. H. Schleifenbaum, P. Wagenblast, W. Meiners, and J. Wagner, 2020, "Influence of keyhole and conduction mode melting for top-hat shaped beam profiles in laser powder bed fusion," Journal of Materials Processing Technology **278**, 116514.

Thampy, V., A. Y. Fong, N. P. Calta, J. Wang, A. A. Martin, P. J. Depond, A. M. Kiss, G. Guss, Q. Xing, R. T. Ott*, et al.*, 2020, "Subsurface cooling rates and microstructural response during laser based metal additive manufacturing," Scientific Reports **10**, 1981.

Thijs, L., K. Kempen, J.-P. Kruth, and J. Van Humbeeck, 2013, "Fine-structured aluminium products with controllable texture by selective laser melting of pre-alloyed AlSi10Mg powder," Acta Materialia **61**, 1809-1819.

Thijs, L., F. Verhaeghe, T. Craeghs, J. V. Humbeeck, and J.-P. Kruth, 2010, "A study of the microstructural evolution during selective laser melting of Ti–6Al–4V," Acta Materialia **58**, 3303-3312.

Thomas, D., 2016, "Costs, benefits, and adoption of additive manufacturing: a supply chain perspective," The International Journal of Advanced Manufacturing Technology **85**, 1857-1876.

Todaro, C. J., M. A. Easton, D. Qiu, D. Zhang, M. J. Bermingham, E. W. Lui, M. Brandt, D. H. StJohn, and M. Qian, 2020, "Grain structure control during metal 3D printing by high-intensity ultrasound," Nature Communications **11**, 142.

Tolochko, N. K., S. E. Mozzharov, I. A. Yadroitsev, T. Laoui, L. Froyen, V. I. Titov, and M. B. Ignatiev, 2004, "Balling processes during selective laser treatment of powders," Rapid Prototyping Journal **10**, 78-87.

Trapp, J., A. M. Rubenchik, G. Guss, and M. J. Matthews, 2017, "In situ absorptivity measurements of metallic powders during laser powder-bed fusion additive manufacturing," Applied Materials Today **9**, 341-349.

Verhaeghe, F., T. Craeghs, J. Heulens, and L. Pandelaers, 2009, "A pragmatic model for selective laser melting with evaporation," Acta Materialia **57**, 6006-6012.

Voisin, T., J.-B. Forien, A. Perron, S. Aubry, N. Bertin, A. Samanta, A. Baker, and Y. M. Wang, 2021, "New insights on cellular structures strengthening mechanisms and thermal stability of an austenitic stainless steel fabricated by laser powder-bed-fusion," Acta Materialia **203**, 116476.

Wang, L., Y. Zhang, and W. Yan, 2020, "Evaporation model for keyhole dynamics during additive manufacturing of metal," Physical Review Applied **14**, 064039.

Wang, X., L. N. Carter, B. Pang, M. M. Attallah, and M. H. Loretto, 2017, "Microstructure and yield strength of SLM-fabricated CM247LC Ni-Superalloy," Acta Materialia **128**, 87-95.

Wang, X., S. Xu, S. Zhou, W. Xu, M. Leary, P. Choong, M. Qian, M. Brandt, and Y. M. Xie, 2016, "Topological design and additive manufacturing of porous metals for bone scaffolds and orthopaedic implants: A review," Biomaterials **83**, 127-141.

Wang, Y., X. Liu, K.-S. Im, W.-K. Lee, J. Wang, K. Fezzaa, D. L. S. Hung, and J. R. Winkelman, 2008, "Ultrafast X-ray study of dense-liquid-jet flow dynamics using structure-tracking velocimetry," Nature Physics **4**, 305-309.

Wang, Y. M., T. Voisin, J. T. McKeown, J. Ye, N. P. Calta, Z. Li, Z. Zeng, Y. Zhang, W. Chen, T. T. Roehling*, et al.*, 2018, "Additively manufactured hierarchical stainless steels with high strength and ductility," Nature Materials **17**, 63-71.

Wei, H. L., J. W. Elmer, and T. DebRoy, 2017, "Crystal growth during keyhole mode laser welding," Acta Materialia **133**, 10-20.

Wei, M., W. J. Ding, G. Vastola, and Y.-W. Zhang, 2022, "Quantitative study on the dynamics of melt pool and keyhole and their controlling factors in metal laser melting," Additive Manufacturing **54**, 102779.

Weingarten, C., D. Buchbinder, N. Pirch, W. Meiners, K. Wissenbach, and R. Poprawe, 2015, "Formation and reduction of hydrogen porosity during selective laser melting of AlSi10Mg," Journal of Materials Processing Technology **221**, 112-120.

Wellershoff, S. S., J. Hohlfeld, J. Güdde, and E. Matthias, 1999, "The role of electron–phonon coupling in femtosecond laser damage of metals," Applied Physics A **69**, S99-S107.

Wilkins, S. W., T. E. Gureyev, D. Gao, A. Pogany, and A. W. Stevenson, 1996, "Phase-contrast imaging using polychromatic hard X-rays," Nature **384**, 335-338.

Williams, P., J. Hadler, F. Maring, R. Lee, K. Rogers, B. Simonds, M. Spidell, M. Stephens, A. Feldman, and J. Lehman, 2017, "Portable, high-accuracy, non-absorbing laser power measurement at kilowatt levels by means of radiation pressure," Optics Express **25**, 4382-4392.

Williams, P. A., K. A. Rogers, J. A. Hadler, A. B. Artusio-Glimpse, and J. H. Lehman, 2021, "Axial force radiometer for primary standard laser power measurements using photon momentum," Metrologia **58**, 015010.

Wolff, S. J., H. Wu, N. Parab, C. Zhao, K. F. Ehmann, T. Sun, and J. Cao, 2019, "*In-situ* high-speed X-ray imaging of piezo-driven directed energy deposition additive manufacturing," Scientific Reports **9**, 962.

Wu, A. S., D. W. Brown, M. Kumar, G. F. Gallegos, and W. E. King, 2014, "An experimental investigation into additive

manufacturing-induced residual stresses in 316l stainless steel," Metallurgical and Materials Transactions A **45**, 6260-6270.

Wu, Z., S. P. Narra, and A. Rollett, 2020, "Exploring the fabrication limits of thin-wall structures in a laser powder bed fusion process," The International Journal of Advanced Manufacturing Technology **110**, 191-207.

Yadroitsev, I., P. Krakhmalev, and I. Yadroitsava, 2014, "Selective laser melting of Ti6Al4V alloy for biomedical applications: Temperature monitoring and microstructural evolution," Journal of Alloys and Compounds **583**, 404-409.

Yan, W., Y. Lu, K. Jones, Z. Yang, J. Fox, P. Witherell, G. Wagner, and W. K. Liu, 2020, "Data-driven characterization of thermal models for powder-bed-fusion additive manufacturing," Additive Manufacturing **36**, 101503.

Yang, J., H. Yu, J. Yin, M. Gao, Z. Wang, and X. Zeng, 2016, "Formation and control of martensite in Ti-6Al-4V alloy produced by selective laser melting," Materials & Design **108**, 308-318.

Yang, K. V., P. Rometsch, T. Jarvis, J. Rao, S. Cao, C. Davies, and X. Wu, 2018, "Porosity formation mechanisms and fatigue response in Al-Si-Mg alloys made by selective laser melting," Materials Science and Engineering: A **712**, 166-174.

Ye, J., S. A. Khairallah, A. M. Rubenchik, M. F. Crumb, G. Guss, J. Belak, and M. J. Matthews, 2019, "Energy coupling mechanisms and scaling behavior associated with laser powder bed fusion additive manufacturing," Advanced Engineering Materials **21**, 1900185.

Zhang, B., S. Liu, and Y. C. Shin, 2019, "In-Process monitoring of porosity during laser additive manufacturing process," Additive Manufacturing **28**, 497-505.

Zhang, H., H. Zhu, X. Nie, J. Yin, Z. Hu, and X. Zeng, 2017, "Effect of Zirconium addition on crack, microstructure and mechanical behavior of selective laser melted Al-Cu-Mg alloy," Scripta Materialia **134**, 6-10.

Zhao, C., K. Fezzaa, R. W. Cunningham, H. Wen, F. Carlo, L. Chen, A. D. Rollett, and T. Sun, 2017, "Real-time monitoring of laser powder bed fusion process using high-speed X-ray imaging and diffraction," Scientific Reports **7**, 3602.

Zhao, C., Q. Guo, X. Li, N. Parab, K. Fezzaa, W. Tan, L. Chen, and T. Sun, 2019, "Bulk-explosion-induced metal spattering during laser processing," Physical Review X **9**, 021052.

Zhao, C., N. D. Parab, X. Li, K. Fezzaa, W. Tan, A. D. Rollett, and T. Sun, 2020, "Critical instability at moving keyhole tip generates porosity in laser melting," Science **370**, 1080-1086.

Zhao, C., Y. Yang, B. Shi, W. Shao, and S. Chen, 2022, "*Operando* monitoring microstructures and defects in laser fusion additive manufacturing of metals (in Chinese)," Chinese Science Bulletin, https://doi.org/10.1360/TB-2022-0439

Zhao, H., and T. DebRoy, 2003, "Macroporosity free aluminum alloy weldments through numerical simulation of keyhole mode laser welding," Journal of Applied Physics **93**, 10089-10096.

Zhu, J.-N., E. Borisov, X. Liang, E. Farber, M. J. M. Hermans, and V. A. Popovich, 2021a, "Predictive analytical modelling and experimental validation of processing maps in additive manufacturing of nitinol alloys," Additive Manufacturing **38**, 101802.

Zhu, Q., Z. Liu, and J. Yan, 2021b, "Machine learning for metal additive manufacturing: predicting temperature and melt pool fluid dynamics using physics-informed neural networks," Computational Mechanics **67**, 619-635.